Operation of a Two- Dimensional Ion Trap Array for Scalable Quantum Computation

by

David Alexander Hucul

A senior honors thesis submitted to

the Department of Physics of

the University of Michigan

College of Literature, Science and the Arts

in fullfilment of the course requirements for Physics 497

in submission for the 2006 W.L. Williams Award

and for the degree of

Honors B.S. in Physics

April 14, 2006

This thesis entitled:
Operation of a Two- Dimensional Ion Trap Array for Scalable Quantum Computation
written by D.A. Hucul
has been approved for submittal by

_____

Prof. Christopher Monroe

Date _____

_____

David A. Hucul

Date _____

The final copy of this thesis has been examined by the research advisor and has been found suitable for completion of the course requirements of Physics 497.

Abstract

Trapped ion systems are promising candidates for scalable quantum computation [1],[2],[3]. Many scalable quantum computing architectures have been proposed, but the one presented here involves using two-dimensional ion trap arrays.

This thesis is concerned with the design, simulation, construction, and operation of a two-dimensional ion trap array. In the trap array, ions can be shuttled linearly, around a corner of a T-junction, through a junction as well as separated and combined in the same trapping zone. This proof of principle experiment shows that it is possible to shuttle ions throughout a two-dimensional array of ion traps in the spirit of the quantum computing scheme proposed by Kielpinski, Monroe, and Wineland [2]. In this particular scheme, ions can be shuttled into interaction zones where ions may be entangled, and storage zones where ions may be sent to store quantum information.

The electric pseudo potential is simulated by constructing basis functions for the trap electrodes. The basis function for each electrode is calculated by simulating the electric pseudo potential with one volt applied to the electrode with the rest of the electrodes grounded. By using symmetry, the number of calculations is greatly reduced.

A discussion concerning adiabatic shuttling is given. Trapped ions are bound in a harmonic oscillator potential and cooled using standard laser cooling techniques. Conditions are given as to how fast the strength of the harmonic well can be changed and how the ion can be accelerated in the potential well while still preserving the number state of the ion during shuttling. The derivation is general and applies to the transport of any cold atoms in a harmonic well.

The inner workings of the T-junction ion trap along with its associated electronic and vacuum components are given. The four shuttling protocols necessary for two dimensional control of trapped ions are presented along with the necessary voltage controls needed to shuttle ions around linearly, to shuttle ions around corners, to separate, and to combine ions in the same trapping zone. A composite protocol which combines the four necessary shuttling protocols is implemented to swap the positions of two trapped ions.

Lastly, a general discussion is given concerning the design challenges and requirements of future experiments to build large, many-zone ion trap arrays for scalable quantum computation in light of what has been learned about trying to have two dimensional control of trapped ions in an 11-zone ion trap array.

Acknowledgements

You can know the name of a bird in all the languages of the world, but when you're finished, you'll know absolutely nothing whatever about the bird... So let's look at the bird and see what it's doing – that's what counts. I learned very early the difference between knowing the name of something and knowing something.

– Richard Feynman

First and foremost I would like to thank Chris Monroe for allowing me to work in his lab as an undergraduate. Despite the fact that I had only finished freshman mechanics when I first asked you if I could work in your lab, you still took me on. I hope that my contribution to the lab has proven meaningful. I could not have fostered my interest in physics without your help. You are exactly the kind of advisor that everyone should have, and I know I would not have the opportunities that are available to me today without your guidance and support.

Secondly, I would like to thank Winfried K. Hensinger for his guidance and patience as I slowly learned about physics, ion trapping, and conducting real scientific research. You are not only an amazing researcher, but you are also an amazing teacher. I am forever in your debt. Thanks for everything Winni.

I need to thank Louis Deslauriers for the advice he has given me over the past couple of years, as well as many others in Chris Monroe's lab, both past and present whom I need to thank as well including Mark Acton, Boris Blinov, Kathy-Anne Brickman, Patricia Lee, Martin Madsen, Peter Maunz, Russell Miller, David Moehring, Steve

Olmschenk, Jim Rabchuk, Jon Sterk, Dan Stick, and Kelly Younge. I also need to thank my fellow undergraduate compatriots Rudy Kohn, Mark Yeo, and Liz Otto. Paul Haljan gave me the excellent advise I needed concerning graduate school. Thanks Paul.

Thanks to all of my friends at the University of Michigan, especially Michael Reim and Daniel Levy. Go Angels! You guys kept me sane during the times when I had an insane amount of work to do. Remember: you guys always have a home where ever I end up.

Lastly, I'd like to thank my parents not only for their funding, but for their support as well. What can I say to the people that brought me in to this world and raised me? Thanks for laying the right path before me and showing me the way.

Contents

Chapter

Figures

Figure

Chapter 1

Introduction

1.1 Trapped Ion Systems as Quantum Computers

A quantum computer is unlike a classical computer in that the information that is stored in a quantum computer may be in a superposition of logical states $\alpha|0\rangle$ and $\beta|1\rangle$, whereas a classical computer has states 0 *or* 1. There are only a few known instances where a quantum computer could have a significant speed advantage over a classical computer; two of the most well-known processes where a quantum computer can offer a significant speed up over a classical computer are Shor's factoring algorithm, and Grover's algorithm which is a search of an unsorted database. For example, Shor proved that a quantum computer can factorize a number in polynomial time as the number becomes larger whereas a classical computer's run time scales exponentially with the size of the number [4]. Before Shor and Grover discovered their algorithms, Feynman pointed out that there is an essential difficulty in simulating quantum systems on classical computers because even for a two level system of 500 particles, the Hilbert space has 2^{500} states. However, he pointed out that it might be possible to overcome these difficulties if one built a quantum computer to simulate quantum systems. If superposition states of all 500 particles can be experimentally achieved, then single operations can act on all 2^{500} states at the same time. After Deutsch's discovery that any physical process can be simulated on a quantum computer[5], a large area of research in quantum information theory became to try to figure out what kinds of problems are

better suited for quantum computers and what kinds of problems are more suited for classical computers [6].

At first glance, a quantum computer seems to hold a great deal of information. Consider a two level quantum system with N particles. Each particle has two states: say spin up ($|1\rangle$) and spin down ($|0\rangle$). The total Hilbert space then has 2^N amplitudes whose states are of the form $|100\ldots\rangle + |010\ldots\rangle + |001\ldots\rangle + \ldots$ However, the measurement of the spin of such states is random! Carefully designed algorithms are needed to get a result out of a quantum computer whose result is meaningful for the problem at hand. Because a quantum computer can essentially be thought of as an analog computer, they are highly suseptible to noise. However, the advent of quantum error correction and fault tolerant computation makes errors possible to deal with[6].

There are many proposed schemes for building a quantum computer using a variety of physical systems. The first quantum computing scheme with trapped atomic ions was proposed by Cirac and Zoller in 1995 [1] which involves using a linear chain of trapped ions in the same trap. Another scheme was proposed by Kielpinski, Monroe, and Wineland [2] and involves the use of trapped ions in an array of ion traps where the arrays of ion traps can be arranged in channels so that ions can be shuttled throughout the entire trap array (see Fig. 1.1). Different regions of the entire trap array could serve different purposes. For example, certain regions of the trap array could serve as memory regions where ions are sufficiently decoupled from the environment so that quantum information can be stored in the different internal or external degrees of freedom of the ions. There could be other regions in the trap array that could serve as interaction zones where ions can be sent to be entangled or have some other logical operation performed on their states.

In trapped ion systems, the $|0\rangle$ and $|1\rangle$ states are typically chosen to be the electronic hyperfine states of a singly ionized hydrogen-like atom with a spin 1/2 nucleus. The general spirit of quantum computation using trapped ions thus far is to modify the

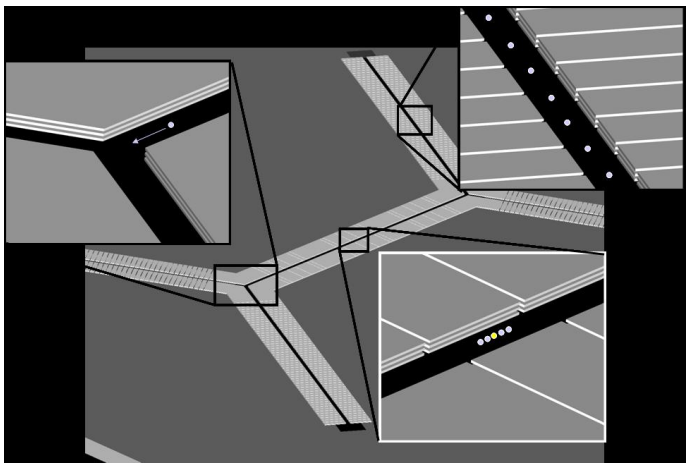

Figure 1.1: Proposed quantum computing scheme with many ions in an array stucture of ion traps[2]. Ions can be shuttled from interaction zones (shown in the center of the figure) where ions may be entangled and other logical gates can be performed to memory zones (depicted in the exploded view in the upper right) where ions can be sent to store quantum information.

hyperfine state of the atom based on the states of other nearby atoms. For example, in a spin 1/2 system, the spin of ion A may be conditionally flipped based on the spin state of its neighbor or neighbors.

1.1.1 DiVincenzo Scalability Requirements

There is much debate as to what should go into building what is deemed a scalable quantum computer. Scalable means that more ions can be added to the system in a straightforward way without exponentially increasing the amount of overhead needed to operate the system. An example of a system that is not scalable is the confinement of hundreds of ions in a single ion trap because it becomes extremely difficult to resolve and cool the vibrational states of the ions. There is a set of generally agreed upon scalablility requirements for a quantum computer put forth by David DiVincenzo[7].

(1) A scalable physical system with well characterized qubits

(2) Initialization of the qubits to a well-known state

(3) A universal set of quantum logic states

(4) Read-out of the qubits

(5) Long coherence times compared to the typical duration of a gate

Many of the items have been demonstrated on this list in various trapped ion systems to some extent. For example, the initialization of qubits to a well known state in trapped ion systems involves optically pumping trapped cadmium ions to hyperfine states and has been widely demonstrated [8]. Many quantum logic gates have been experimentally demonstrated [9],[10], [11], [8], [12] and efficient readout of cadmium qubit states has demonstrated to various levels [13]. Long coherence times have been observed that are much longer than the typical duration of a gate; a 15 second spin coherence time has even been observed [14].

The primary work for this thesis is based on development of the first item in DiVencenzo's list and has received lots of attention as of late [15],[16],[17],[18]. The idea of how to physically connect up a quantum system is a very interesting question. There are many proposals about how to do this, but they generally involve two basic principles in trapped ion systems: the ability to interconvert between flying qubits and stationary qubits, and the ability to faithfully transfer flying qubits from location to location. The jargon "flying qubit" typically refers to photons, and entanglement between photons and ions has been demonstrated by Blinov et al [17]. However, flying qubits need not be photons; shuttling ions can be considered a means spatially moving quantum information despite the slower "flying" speed. Shuttling ions may be a better way to *faithfully* transmit quantum information as opposed to single photons in certain instances.

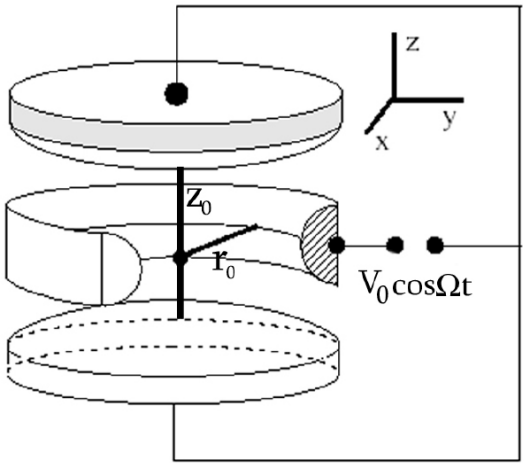

Figure 1.2: An idealized Paul trap. The center ring is a distance r_0 from the center of the trap and carries RF voltage with angular frequency Ω. The endcap electrodes confine the ion in the z-direction are located a distance z_0 away from the center of the trap as shown in the figure and have a voltage difference of $U_0 + V_0 cos(\Omega t)$ between the ring and endcaps. Note that in an ideal Paul trap, the endcaps are hyperbolic.

1.2 Ion Dynamics in an Ion Trap

It is impossible to confine charged particles in free space using static electric fields because the divergence of the electric field in free space is zero. It is possible to confine a charged particle in all three spatial directions using time-varying electric fields [19]. A classic ion trap geometry consists of hyperbolic trap electrode endcaps where static voltages are applied to confine ions in the z-direction, and a ring that carries RF which provides confinement in the xy plane. An ideal Paul trap can be seen in Fig. 1.2. The potential in the ion trap is:

$$V(\vec{r}, t) = U_0 + V_0 cos(\Omega t) \frac{r^2 - 2z^2}{d_0^2} \tag{1.1}$$

where r is the radial coordinate, z is the height above or below the center of the ring electrode, $\Omega/2\pi$ is the RF frequency, d_0 is a characteristic ion trap parameter $d_0 = (r_0^2 + 2z_0^2)^{1/2}$. The equations of motion for a particle with mass m and charge e in the

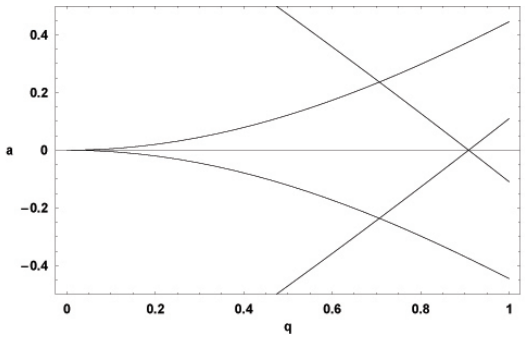

Figure 1.3: Mathieu stability paramters for idealized Paul trap with hyperbolic electrodes. The bounded region in the center of the plot shows the parameters with bounded solutions to the Mathieu equations (Eq. 1.5)

r and z directions are:

$$\frac{\partial^2 r}{\partial t^2} + \frac{2e}{md_0^2}(U_0 + V_0 cos(\Omega t))r = 0 \tag{1.2}$$

$$\frac{\partial^2 z}{\partial t^2} - \frac{4e}{md_0^2}(U_0 + V_0 cos(\Omega t))z = 0 \tag{1.3}$$

A change of variables ($\Omega t/2 = \zeta$), these equations can be changed into Mathieu equations with the following characteristic a-q parameters [19]:

$$a_r = -\frac{a_z}{2} = \frac{8eU_0}{md_0^2\Omega^2}; q_r = -\frac{q_z}{2} = \frac{4eV_0}{mr_0^2\Omega^2}; \zeta = \frac{\Omega t}{2} \tag{1.4}$$

Substitution of the parameters in Eq. 1.4 and the change of variables into Eq. 1.2, the ion's motion is now represented by two Mathieu equations.

$$\frac{\partial^2 r}{\partial \zeta^2} + (a_r - 2q_r cos(2\zeta))r = 0 \tag{1.5}$$

$$\frac{\partial^2 r}{\partial \zeta^2} + (a_z - 2q_z cos(2\zeta))z = 0 \tag{1.6}$$

These differential equations are well studied and numerical solutions are known [20]. The motion of an ion is bounded or unbounded based on the parameters a and q. It is possible to plot regions in the a-q plane that result in bounded motion.

It is possible to break up the motion of the ion in to a time-averaged, slow, secular motion and a fast oscillation. In the radial direction, the ion's motion may be thought

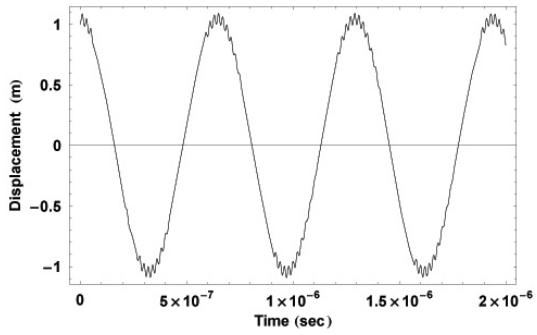

Figure 1.4: Numerical integration of Mathieu equations of motion in an ideal Paul trap. The equations of motion of an ion of mass m and charge e are in Eq. 1.5. Numerical integration of these equations shows a large secular motion of a harmonic oscillator that is modulated by the RF drive frequency Ω. The values for a and q in this plot are 0 and 0.175 respectively.

of as a sum of secular motion r' and micrmotion r_μ so that $r = r' + r_\mu$. After setting $U_0 = 0$ for convenience, Eq. 1.2 in the r-direction breaks up into secular motion and micromotion.

$$\frac{\partial^2 r'}{\partial t^2} + \frac{\partial^2 r_\mu}{\partial t^2} = \frac{4e}{md_0^2} V_0 cos(\Omega t)(r' + r_\mu) \tag{1.7}$$

The secular motion is typically much larger than the micromotion, so it is a good approximation that $r' \gg r_\mu$. The micromotion is typically at a higher frequency (the RF drive frequency), so $\ddot{r}_\mu \gg \ddot{r}'$. With these two approximations, Eq. 1.7 becomes

$$\frac{\partial^2 r_\mu}{\partial t^2} = \frac{4e}{md_0^2} V_0 cos(\Omega t) r' \tag{1.8}$$

Integration twice yields:

$$r_\mu = -\frac{4e}{md_0^2\Omega^2} V_0 cos(\Omega t) r' \tag{1.9}$$

The sum of the secular and micromtion is then:

$$r = r' - \frac{4e}{md_0^2\Omega^2} V_0 cos(\Omega t) r' \tag{1.10}$$

Eq. 1.10 can be put back in to Eq. 1.2 to yield:

$$\frac{\partial^2 r}{\partial t^2} = \frac{4e}{md_0^2} V_0 cos(\Omega t) r' - \frac{8e^2}{md_0^4\Omega^2} V_0^2 cos^2(\Omega t) r' \tag{1.11}$$

To extract the secular motion behavior of the ion, the above equation can be averaged over one RF period because the RF period is much shorter than the period of secular motion.

$$\begin{aligned}\langle \ddot{r} \rangle = \frac{\Omega}{2\pi}\int_0^{\frac{2\pi}{\Omega}} \frac{\partial^2 r}{\partial t^2} dt &= \frac{\Omega}{2\pi}\int_0^{\frac{2\pi}{\Omega}} \Big(\frac{4e}{md_0^2} V_0 cos(\Omega t) r - \frac{8e^2}{m^2 d_0^4 \Omega^2} V_0^2 cos^2(\Omega t) r\Big) dt \\ &= -\frac{4e^2 V_0^2}{m^2 d_0^4 \Omega^2} r \end{aligned} \tag{1.12}$$

In Eq. 1.12, the micromotion term averages to zero because the cosine term averages to zero. The resulting averaging yields the equation of motion for a simple harmonic oscillator. To make this more explicit:

$$\langle \ddot{r} \rangle = -\frac{4e^2 V_0^2}{m^2 d_0^4 \Omega^2} \langle r \rangle \tag{1.13}$$

This is the equation of motion for a simple harmonic oscillator with secular frequency ω :

$$\omega_r = \frac{2eV_0}{md_0^2\Omega} \tag{1.14}$$

An approximation for this equation of motion is a product of the secular frequency and a term which represents the micromotion of the ion. Similar analysis of the equation of motion in the z-direction yields a harmonic potential with secular frequency $\omega_z = \sqrt{2}\omega_r$. A plot of this motion can be seen in Fig. 1.5 and shows the same qualitative behavior as the numerical integration of Eq. 1.2; the ion oscillates back and forth with a slow secular frequency that is modulated by micromotion at the RF drive frequency.

$$r(t) \approx cos(\omega t)\Big(1 - \frac{4e}{md_0^2\Omega^2}(U_0 + V_0 cos(\Omega t))\Big) \tag{1.15}$$

1.3 A Model Ion Trap: Rotating Saddle Surface

A pedogogical example of an ion trap potential is a rotating hyperbolic paraboloid (a saddle surface) on which a ball can be trapped. A symmetric saddle surface can in general be descibed by $f(x, y) = \eta(x^2 - y^2)$ where η is a geometrical parameter that

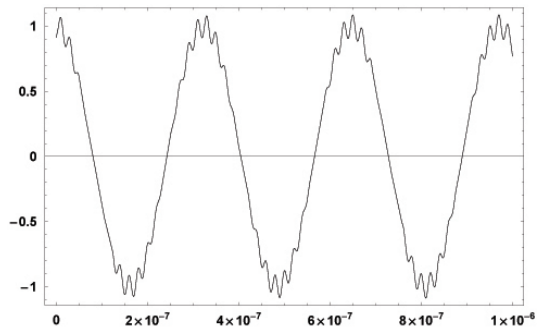

Figure 1.5: Plot of ion motion in Eq. 1.15 vs. time in seconds. The ion's motion is that of s simple harmonic oscillator that is modulated by the RF drive frequency. The amplitude of oscillation is normalized.

specifies the curvature of the saddle and has units of inverse length. As pointed out by Thompson et al [21], the analogy between a rotating saddle surface and the effective ponderomotive potential of an ion trap is not exact. The ponderomotive potential in an ion trap is that of a saddle in two dimensions, but the time evolution of the potential is one that flaps up and down. The mechanical rotating saddle does not have a flapping potential; the potential rotates (see Fig. 1.6). The mechanical analogue also differs from an actual ion trap in other ways. The rotating saddle and ball system has the effects of friction and rolling because the ball is in contact with a hard surface. Despite the seemingly large differences between the two systems, a ball on a rotating saddle surface is analogous to an ion trap and was referred to by W. Paul in his Nobel lecture concerning his work in ion trapping [22]. As will be shown, simulations of Lagrange's equations of motion show that a ball will become trapped in rotating saddle potential and will undergo motion that is qualitatively similar to a trapped ion.

The potential of the system is [21]:

$$V(x,y,t) = mg\eta\Big((x^2-y^2)cos(2\Omega t) + 2xysin(2\Omega t)\Big) \tag{1.16}$$

In Eq. 1.16, m is the mass of the ball in the well, g is the gravitational acceleration, Ω is the angular drive frequency of the spinning saddle, and η is a geometrical constant with units length that specifies the curvature of the saddle surface. The Lagrangian of

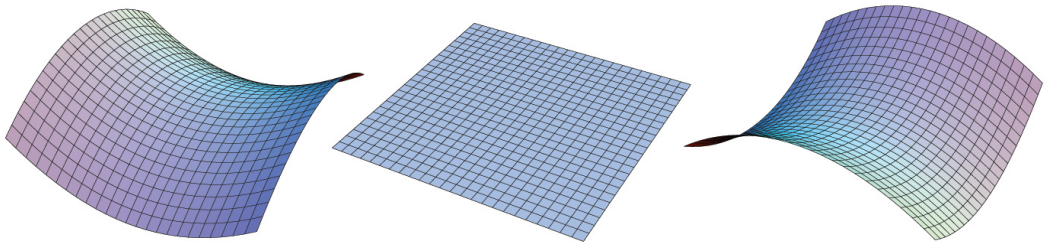

Figure 1.6: The flapping potential is that of a real ion trap system while the rotating potential is from the mechanical analogue of an ion trap. The above figure shows the time evolution of the potential of a real ion trap. The potential does not rotate in time but instead flaps up and down and is flat half way through the RF period. A real rotating trap also differs in that there is a damping force due to friction as well as the effect of a mass rolling around on the surface.

the system is:

$$L = \frac{1}{2}(\dot{x}^2 + \dot{y}^2) - g\eta\Big((x^2 - y^2)cos(2\Omega t) + 2xysin(2\Omega t)\Big) \tag{1.17}$$

There is no $\dot{z}$ term because the ball is being a priori constrained to the surface of the rotating saddle so the z-direction is not an independent coordinate. This is assumed to be true because for slow enough rotations; the ball does not leave the surface of the rotating saddle. The specified Lagrangian also assumes that the ball in the saddle surface only slides and does not roll. Lagrange's equations of motion for a sliding, non-rolling particle that is constrained to move on the surface of a spinning saddle potential are:

$$\ddot{x} = -2g\eta\Big(xcos(2\Omega t) + ysin(2\Omega t)\Big) \tag{1.18}$$

$$\ddot{y} = -2g\eta\Big(xsin(2\Omega t) - ycos(2\Omega t)\Big) \tag{1.19}$$

$$z = \eta(x^2 - y^2) \tag{1.20}$$

As is pointed out in the literature, it is possible to analytically solve these coupled differential equations [21], but the utility of the analytical solutions of Eq. 1.18-1.20 is somewhat diminished due to the fact that friction and rolling are neglected. However,

the analytical solution of Lagrange's equations of motion yields a condition for whether or not the motion of the ball is bounded in the trap neglecting friction and rolling. Making the coordinate transformation $\zeta = \Omega t$:

$$\frac{\partial^2 x}{\partial \zeta^2} = -2q\Big(xcos(2\zeta) + ysin(2\zeta)\Big) \tag{1.21}$$

$$\frac{\partial^2 y}{\partial \zeta^2} = -2q\Big(xsin(2\zeta) - ycos(2\zeta)\Big) \tag{1.22}$$

In Eq. 1.21-1.22, $q = g\eta/\Omega^2$. As pointed out in [21], it is possible to solve these two coupled differential equations by defining $z = x + iy$ and adding Eq. 1.21 and i times 1.22 to yield:

$$\frac{\partial z}{\partial \zeta} + 2qz^* e^{2i\zeta} = 0 \tag{1.23}$$

The solution to this differential equation is of the form:

$$z(\zeta) = f(\zeta)e^{i\zeta} \tag{1.24}$$

This equation for z (or z^*) can be substituted back into Eq. 1.23 to yield two differential equations that are second order in either $f(\zeta)$ or $f^*(\zeta)$. The f^* can be eliminated by subsitution to yield:

$$\frac{\partial^4 f(\zeta)}{\partial \zeta^4} + 2\frac{\partial^2 f(\zeta)}{\partial \zeta^2} + (1 - 4q^2)f(\zeta) = 0 \tag{1.25}$$

The solution to Eq. 1.25 can be expressed as a linear combination of four exponentials whose coefficients depend upon the intial conditions of the system:

$$f(\zeta) = Ae^{\beta_+ \zeta} + Be^{-\beta_+ \zeta} + Ce^{\beta_- \zeta} + De^{-\beta_- \zeta} \tag{1.26}$$

$$\beta_\pm = \sqrt{\pm 2q - 1} \tag{1.27}$$

Clearly the only way to prevent a solution that is unbounded is if all of the exponentials are complex. This leads to the requirement that:

$$2q = \frac{2g\eta}{\Omega^2} \leq 1 \tag{1.28}$$

As pointed out by Thompson [21], the analogy of a ball in a spinning saddle to an ion trap may become clear. If Eq. 1.28 is true, then the ball is trapped since the motion is bounded. To see the connection between a ball confined to a spinning saddle surface and an ion trap, assume that the motion of a sliding, non-rolling ball on the spinning saddle surface well can be broken up into two terms $z = Z + \delta$ where Z describes the secular motion of the ball while δ describes a superimposed micromotion of the ball. Plugging this in to Eq. 1.23:

$$\frac{\partial^2 Z}{\partial \zeta^2} + \frac{\partial^2 \delta}{\partial \zeta^2} + 2q(Z^* + \delta^*)e^{2i\zeta} = 0 \tag{1.29}$$

Since the frequency of oscillation of the micromotion δ is high compared to Z, its second derivative with respect to ζ is generally much greater than that of the secular motion. The secular motion Z is generally much larger than the micromotion δ. Both of these facts mean that δ^* and $\partial^2 Z/\partial\zeta^2$ are insignificant in Eq. 1.29.

$$\frac{\partial^2 \delta}{\partial \zeta^2} = -2qZ^* e^{2i\zeta} \tag{1.30}$$

Integration of the above equation yields:

$$\delta = \frac{1}{2} qZ^* e^{2i\zeta} \tag{1.31}$$

The complex conjugate of the above equation for δ may be taken and plugged into Eq. 1.29 to yield:

$$\frac{\partial^2 Z}{\partial \zeta^2} + \frac{\partial^2 \delta}{\partial \zeta^2} + 2qZ^* e^{2i\zeta} + q^2 Z = 0 \tag{1.32}$$

Since the micromotion of the system is fast compared to the secular motion, an average value of Z may be taken. The fast micromotion term $\partial^2\delta/\partial\zeta^2$ averages to zero while the $2qZ^*e^{2i\zeta}$ term also averages to zero because Z^* hardly varies while the exponential averages to zero. The only significant terms remaining are:

$$\frac{\partial^2 Z}{\partial \zeta^2} + q^2 \langle Z \rangle = 0 \tag{1.33}$$

$$\langle \ddot{Z} \rangle + q^2 \Omega^2 \langle Z \rangle = 0 \tag{1.34}$$

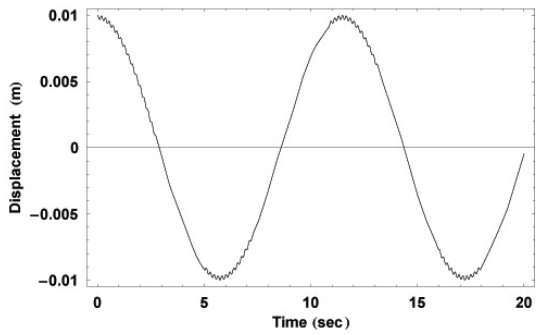

Figure 1.7: Simulation of the motion of a sliding, non-rotating ball on a rotating saddle surface with curvature η =0.962 m^{-1} that is rotating at 2.7 Hz to give a trapping parameter of $q = 0.033$. The ball is initially at rest and is displaced from equilibrium by 10 cm. Numerical integration of Eq. 1.18 shows a characteristic secular frequency that is modulated by micromotion whose effect becomes noticeable when the ball is at the extrema of its motion.

The solution to Eq. 1.34 is harmonic motion with a frequency $q\Omega/2\pi$ Hz. According to Thompson et al [21], this approximation begins to break down when the trapping parameter q is greater than about 0.15. The behavior of a sliding, non-olling ball in a rotating saddle surface displays some of the properties of an ion trap. The pseudo-potential approximation of the rotating saddle surface leads to an effective harmonic bowl as can be seen in Eq. 1.34. The simulated motion of the ball displays similar dynamics to that of a trapped ion in a flopping potential as can be seen in Fig. 1.7. Note that the time evolution of an ion in an ion trap and a ball confined to slide without rolling on a rotating saddle surface displays a large secular motion and a fast micromotion. It is even possible to feel the ponderomotive potential of the rotating saddle surface by placing a finger on the center of the saddle surface as it rotates and moving the finger radially outward.

A model rotating saddle was built that has trapping times of order minutes and a record trapping time of five and a half minutes. The hyperbolic paraboloid surface was machined out of high density polyethylene to $\eta = 0.962m^{-1}$ to give a trapping parameter of $q = 9.44/\Omega^2$. The trap is powered by a record player motor that rotates

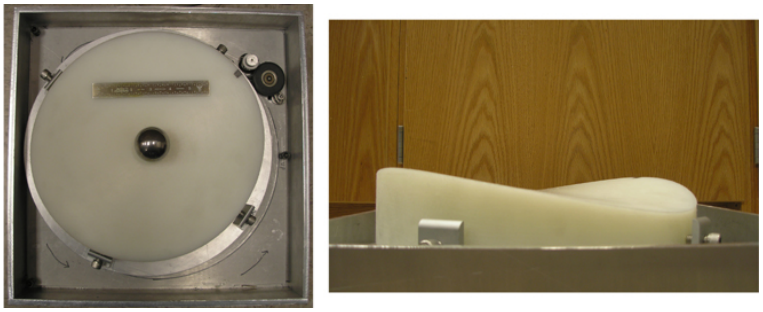

Figure 1.8: Top and side view of rotating saddle surface trap. The trap rotates at frequency $\Omega/2\pi = 2.7$ Hz and has a geometrical factor $\eta = 0.962$ m^{-1} to give a trapping parameter of $q = 0.033$.

the trap at $\sim$ 2.7 Hz so that $q = 0.033$, well in the limit that $2g\eta/\Omega^2 \leq 1$ to give bounded motion if the trapped ball were only sliding and not rolling and well within the pseudopotential approximation of $q \leq 0.15$.

Unlike the trap reported in [21] that had trapping lifetimes of order 10 seconds, the rotating saddle with $q = 0.033$ had trapping lifetimes as long as 5.5 minutes. Other than the different geometrical parameter η, the rotation frequency of the trap was almost a factor of 2 higher than the Calgary trap.

As reported by Thompson et al [21], the trapping lifetime strongly depends on the angle of tilt of the saddle. For small tilt angles, it was possible to find a "sweet spot" where the ball could be trapped for several minutes. These long trapping times were achieved by first allowing the ball to spin up so that the tangential velocity associated with the rotation of the ball matched the tangential velocity of the rotating saddle.

The trapping lifetime also strongly depends on the ball used in the trap. Several different size steel ball bearings and a bowling ball were used to test trapping lifetimes. The larger balls were trapped much longer than smaller balls by orders of magnitude. For example, a steel ball bearing with a 1/8 inch diameter stays in the trap for about 1 second, a half inch diameter ball bearing can stay trapped for up to a minute. A one inch diameter steel ball bearing had up to a 5.5 minute lifetime.

Chapter 2

Electric Potentials and Ion Motion in Ion Trap Arrays

2.1 Simulation of the Electric Pseudo Potential in Ion Trap Arrays via Basis Functions

In order to have control over hundreds or thousands of trapped ions, it is necessary to be able to simulate the electric potential in an array of ion traps. Many quantum computing schemes involve shuttling ions between interaction zones and entanglement zones, so it becomes necessary to simulate the potential due to the time varying voltages of the control electrodes that are used to shuttle ions. For large ion trap arrays, the cost of calculating the electric field due to many trap electrodes and at each point in time during a shuttling operation is prohibitive. An alternative approach to simulating the electric potential in large ion trap arrays is to develop a set of "basis functions" for the electric potential, and scale them by appropriate multiplicative factors that represent the time-varying voltages of the control electrodes. The total electric potential in a many-array ion trap is then the sum of the scaled basis functions. The reason that this approach saves simulation time is that only the basis functions need to be accurately simulated because once the basis functions for the electric potential is known, it is simple to calculate the electric potential for any arbitrary voltage configuration of the electrodes. The only draw back to this approach is that the basis functions are for a fixed geometry; if a different trap geometry is to be explored (this includes electrode sizing and spacing), the basis functions must be re-calculated.

As can be seen in the subsequent section, the basis functions are constructed by grounding every trap electrode and applying a unit voltage to a single control electrode. This proces is repeated for every individual electrode in the ion trap array, although the total number of basis function simulations that need be calculated can be reduced if the ion trap has some planes of symmetry.

2.1.1 Justification for the Basis Function Technique

It is possible to simulate the potential in any complex, multi-zone ion trap by developing electric potential basis functions. The electric potential for any arbitrary voltage configuration of the trap electrodes can then be built up as a linear combination of the basis functions. The electric potential of any arbitrary charge configuration with Dirichlet boundary conditions at a particular moment in time can be written as[23]:

$$\Phi(\vec{x}) = \frac{1}{4\pi\epsilon_0}\int_V \rho(\vec{x}\,')G(\vec{x},\vec{x}\,')d^3x' - \frac{1}{4\pi}\oint_S \Phi(\vec{x}\,')\frac{\partial G(\vec{x},\vec{x}\,')}{\partial n'}da' \tag{2.1}$$

In Eq. 2.1, the first integral is an integral over the volume interior to the boundary with the appropriate symmetric Green function $G(\vec{x},\vec{x}\,')$. Inside of an ion trap, there is no free charge so $\rho(\vec{x}\,') = 0$ making the first term of Eq. 2.1 zero. The second integral is an integral over the surface of the boundary only, i.e. the trap electrodes. $\Phi(\vec{x}\,')$ is the potential on the surface of each electrode multiplied by the outward normal derivative of the Green function with respect to the surface n', the normal direction to the trap electrodes. It is possible to write the potential that is specified on every trap electrode as a sum of potentials on each individual electrode.

$$\Phi(\vec{x}\,') = \sum_i \Phi_i(\vec{x}\,') \tag{2.2}$$

This changes Eq. 2.1 to

$$\Phi(\vec{x}) = -\frac{1}{4\pi}\sum_i \oint_{S_i} \Phi_i(\vec{x}\,')\frac{\partial G_i(\vec{x},\vec{x}\,')}{\partial n_i'}da' \tag{2.3}$$

$$= -\frac{1}{4\pi}\oint_{S_1} \Phi_1(\vec{x}\,')\frac{\partial G_1(\vec{x},\vec{x}\,')}{\partial n_1'}da' - \frac{1}{4\pi}\oint_{S_2} \Phi_2(\vec{x}\,')\frac{\partial G_2(\vec{x},\vec{x}\,')}{\partial n_2'}da'$$

$$- \frac{1}{4\pi}\oint_{S_3} \Phi_3(\vec{x}\,')\frac{\partial G_3(\vec{x},\vec{x}\,')}{\partial n_3'}da' - ... \tag{2.4}$$

As can be seen in Eq. 2.3, the total electric potential $\Phi(\vec{x})$ is a sum of the potentials produced by each electrode surface individually. Secondly, the form of Eq. 2.3 is such that if every electrode potential is set to 1 volt times a constant a_i, the potential becomes

$$\Phi(\vec{x}) = -\sum_i \frac{a_i}{4\pi}\left(\oint_S I(\vec{x}\,')\frac{\partial G(\vec{x},\vec{x}\,')}{\partial n'}da'\right)_i \tag{2.5}$$

where $I_i(\vec{x}\,')$ is the boundary of the i-th electrode with magnitude 1 volt. Eq. 2.5 can be interpreted as a linear combination of basis vectors (the quantity in parantheses of Eq. 2.5) multiplied by coefficients $-a_i/4\pi$. The a_i can be adjusted to any arbitrary voltage and the electric potential can then be computed by multiplying the a_i by the basis vectors defined in Eq. 2.5. When shuttling ions, the a_i will become $a_i(t)$, so the electric potential can be calculated as a function of time simply by summing the basis functions by a scaled coefficient that represents the voltage on the i-th electrode as a function of time. Each individual basis function can be calculated by applying 1 volt to a single electrode and grounding all other electrodes.

During a shuttling operation, it is possbile to separate the potential into a product of time-dependent and space-dependent functions because the wavelength of the electromagnetic disturbances produced by the transient ($\sim 10^6 Hz$) and rf fields ($\sim 10^7 Hz$) is on the order of tens or hundreds of meters, while the trap dimensions are typically of order millimeters. Thus, the change of the potential in the trap region is uniform throughout, and essentially simultaneous with the change in voltage on the electrode.

2.1.2 Building up Basis Functions in Symmetric Ion Trap Arrays

Having a certain amount of symmetry in ion trap arrays is very helpful in reducing the total number of basis functions that are necessary to calculate. Two important symmetry operations to consider are rotational symmetry and mirror plane symmetry. Consider a three-layer T-junction ion trap array which has a C_2 principle rotation axis as well as one non-trivial mirror plane that passes directly through the central RF layer. This dramatically reduces the number of simulations needed to construct the basis for the electric pseudo-potential of the entire trap array. In this particular geometry, by simulating the potential of one electrode with one volt applied to it with all other electrodes grounded, one immediately knows the effect of simulating the voltage of the electrode of the electrode on the opposite side of the C_2 axis as well as effect of applying voltage to the electrode on the opposite side of the RF layer because of the mirror plane. The effect of applying voltage to the electrode that is both opposite the C_2 axis and on the opposite side of the RF layer is known by symmetry as well via the successive application of a reflection and C_2 rotation. In other words, for every one electrode basis function that is simulated, four basis functions are extracted. The exception to this is the RF layer because it lies on the reflection plane and the RF layer is monolithic in the T-trap. In a three layer, single X-junction ion trap, it is possible to extract 16 basis functions for every one basis function simulation of an electrode that is not on the corner of the junction and 8 basis functions for an electrode that is on the corner. The reason that a different number of basis functions may be extracted in the X-junction geometry is because some of the electrodes in the X-junction geometry lie along the mirror planes. The larger number of extracted basis functions is due to the higher degree of symmetry in a three-layer, X-junction ion trap than in a three-layer T-junction ion trap. More precisely, the three layer-layer X-junction has less geometrically distinct electrodes than a three-layer T-junction trap array.

Geometrically distinct electrodes are any two electrodes that cannot be brought onto each other via any number of symmetry operations associated with the symmetries of the ion trap array. For example, in the three-layer T-junction ion trap example, if an electrode cannot be brought to the location of another electrode by any combination of C_2 rotations about the principle axis or reflections about the mirror plane through the RF layer, the two electrodes are geometrically distinct and require separate simulations to construct their basis functions. As ion trap arrays grow larger, more basis function calculations are necessary to simulate the electric pseudo-potential but the construction of trap arrays with high degrees of symmetry greatly reduces the number of basis function calculations that need be carried out.

Note that this reduction in the number of simulations required to fully construct the electric pseudo-potential basis applies to the symmetry of the entire array of ion traps. In other words, connecting two, three-layer X-junction ion traps and simulating the potential with one non-grounded electrode yields either 16, 8, or 4 basis functions basis functions depending on which electrode is simulated. If many X-junction ion traps are to be connected to form a large square array of ion traps, it may seem like symmetry does not help that much if there are thousands of geometrically distinct electrodes. However, if the trap array grows sufficiently large, the electrodes near the center of the array are approximately geometrically indistinct because the trap looks approximately isotropic to the electrodes that are near the center of the array. A single basis function simulation may yield an accurate enough approximation of the electric pseudopotential basis of many trap electrodes.

2.2 Simulation of Ion Shuttling in Ion Trap Arrays

Using the calculated basis functions, it is possible to build up arbitrary time dependent potentials in ion trap arrays. Since the gradient of the pseudo-potential is proportional to the force on the ion, it is straightforward to write down the classical

equations of motion for the ion.

$$\sum_{i=1}^{3} \ddot{\mathbf{x}}_i + \frac{q}{m} \nabla_i \Phi(\mathbf{x}, t) = 0 \tag{2.6}$$

The classical equations of motion in Eq. 2.6 do not consider micromotion because $\Phi(\mathbf{x}, t)$ is the pseudo-potential. It is not necessary to simulate ion shuttling quantum mechanically because the action of motion of the ion during typical shuttling operations is much larger than $\hbar$ ([25],[16]).

There are many possible numerical methods that could be used to simulate Eq. 2.6, but the method that was primarily used to simulate the classical motion of the ion to successfully shuttle an ion around the corner of a T-junction ion trap array was the Bulirsch-Stoer method. This numerical method yields high-accuracy solutions very efficiently, although it does not yield low-accuracy solutions very efficiently and thus would be a poor choice for doing rough simulations[26]. This numerical method does not work very well for rough or discontinous potentials either. A full explanation of the Burlish Stoer method and other numerical methods and how they apply to simulating shuttling ions throughout an array of ion traps is presented by M. Yeo in his undergraduate honors thesis[27].

2.3 Adiabatic Shuttling

The ability to shuttle ions adiabatically may turn out to be very important in a quantum computer. Many proposed algorithms thus far involve coupling the internal and external degrees of freedom of the ion; the Molmer-Sorenson gate couples the spin of the ion to its motion. Adiabatically shuttling ions ensures that the ions remain in the same motional state throughout the shuttling process which may be vital to preserving quantum information.

2.3.1 Theory of Adiabatic Shuttling

There are many definitions of what it means for a process to be "adiabatic," but for the purposes of ion trap quantum computing, we will focus on the interpretation that during a linear shuttling process, not enough energy is added to the system to allow for transitions to other quantum states. If a system starts out in the state Ψ_n and there are various excited states Ψ_m, of particular interest are the following two conditions:

$$|\langle\Psi(t)|\Psi_n^f\rangle|^2 \approx 1$$
$$|\langle\Psi(t)|\Psi_m^f\rangle|^2 \approx 0 \tag{2.7}$$

These conditions say that when an ion starts out in some ground state, the quantum state of the ion does not change after the ion is shuttled in some amount of time T. Classically, one can think of this as having a marble oscillating in a bowl. If the bowl is carried around slowly enough, marble will not acquire much energy and its amplitude of oscillation will not increase. This is not the only demand that will be made on the system though. Since the calculation of $|\langle\Psi(T)|\Psi_m^f\rangle|^2 \approx 0$, and since this calculation will be carried out to first order, we will demand that there is a first order cancellation of the transition probablility from state $|\Psi(T)\rangle$ to the state $|\Psi_n^f\rangle$.

The potential of a harmonic oscillator with a translating minimum point in time and whose curvature is modulated in time is given by:

$$V(x,t) \quad = \quad \frac{1}{2}m\omega^2(t)[x - x_0(t)]^2 \tag{2.8}$$

It is convienent to transform in to the frame of the moving harmonic oscillator and define a new coordinate $s = x - x_0(t)$. Doing this introduces a virtual force which modifies the potential in Eq. 2.8 because $x_0(t)$ may have non-zero second time derivatives; the potential could be accelerating. Following the treatment of the adiabatic approximation in Griffiths[28], it is convienent to write the potential as a product of spatially dependent

terms and time-dependent terms in the moving frame:

$$V'(x,t) = \frac{1}{2}m\omega^2(t)s^2 + m\ddot{x}_0(t)s \tag{2.9}$$

$$= \frac{1}{2}m\omega_0^2[1+f(t)]s^2 + m\ddot{x}_0(t)s \tag{2.10}$$

In Eq. 2.9, the function $f(t)$ modulates the potential so that the initial secular frequency ω_0 changes in time ($f(0) = 0$). The Hamiltonian of the system in the moving frame is then:

$$H = \underbrace{\frac{p^2}{2m} + \frac{1}{2}m\omega_0^2 s^2}_{H_0} + \underbrace{\frac{1}{2}m\omega_0^2 f(t)s^2 + m\ddot{x}_0(t)s}_{H'} \tag{2.11}$$

Eq. 2.11 is a sum of the unperturbed harmonic oscillator Hamiltonian H_0 and a perturbation Hamiltonian H'. Note that the momentum operator does not need to be modified since $s = x - x_0(t)$, so $\partial_x = \partial_s$.

Suppose that the state of the system is Ψ_n^i where n is the initial eigenstate of the unperturbed Hamiltonian, and suppose that Ψ_m^f is the m-th eigenstate of the perturbed Hamiltonian at the end of the shuttling time $t = T$. As discussed earlier, during a shuttling operation it may be desirable to prevent the ion from making a transition from the n-th eigenstate of the initial, unperturbed Hamiltonian a different, m-th eigenstate of the final Hamiltonian. In other words, although the position representation of the ion may be different at the end of the shuttling operation ($\Psi_n^i \neq \Psi_n^f$), the number state of the ion is the same after the ion is shuttled. The final available eigenstates in the position representation Ψ_n^f of the ion in the moving frame can be written in terms of the initial wavefunction Ψ_n^i using first order time independent perturbation theory.

$$\Psi_n^f(s) \approx \Psi_n^i(s) + \sum_{k\neq n} \frac{W_{kn}(s,T)}{\hbar\omega_{kn}}\Psi_k(s) \tag{2.12}$$

The time independent perturbations are straight forward to write out. If the total shuttling time is T, then:

$$W_{kn} = \frac{1}{2}m\omega_0^2\langle k|s^2|n\rangle f(T) + m\langle k|s|n\rangle\ddot{x}_0(T) \tag{2.13}$$

$$= W_{1,kn}f(T) + W_{2,kn}\ddot{x}_0(T)$$

The matrix elements in Eq. 2.13 are easy to calculate using raising and lowering operators [24] and yields the selection rule $\Delta n = 0, \pm 1, \pm 2$. The total shuttling time T can refer to one of several things. In order for Eq. 2.12 to be valid, the initial and final Hamiltonians cannot be much different from each other between t = 0 and t = T because Eq. 2.12 assumes that the perturbation is small. In general the final Hamiltonian could be drastically different from the initial Hamiltonian, in which case Eq. 2.13 is not valid because there is no longer a small perturbation. However, in principle the total shuttling time can be broken up into a small interval of time T that makes the perturbation Hamiltonian small. Each small interval T can then be used in succession to track the available eigenstates of the system as the Hamiltonian evolves in time.

If the total shuttling time is a length T, the wavefunction $\Psi(T)$ can be written down using first order time dependent perturbation theory. For an ion initially in the n-th eigenstate of a system:

$$\Psi(s,t) = \sum_{\ell} c_\ell(t) \Psi_\ell e^{-i\omega_\ell t} \tag{2.14}$$

The time dependent coefficients in Eq. 2.14 can be written out explicity for the case when $n = \ell$ and when $n \neq \ell$. For mathematical clarity, define the initial acceleration of the potential $\ddot{x}_0(0)$ and $f(0) = 0$ as before.

$$n = \ell : c_\ell(t) = 1 - \frac{i}{\hbar} W_{1,nn} \int_0^t f(t')dt' \tag{2.15}$$

$$n \neq \ell : c_\ell(t) = -\frac{i}{\hbar} W_{1,\ell n} \int_0^t f(t') e^{i\omega_{\ell n} t'} dt' - \frac{i}{\hbar} W_{2,\ell n} \int_0^t \ddot{x}_0(t') e^{i\omega_{\ell n} t'} dt' \tag{2.16}$$

The quantity $\omega_{\ell n}$ is equal to $\omega_\ell - \omega_n$. In Eq. 2.15, there is no matrix element from the $W_{2,nn}$ term because the selection rule for the $W_{2,nn}$ is $\Delta n = \pm 1$. Using integration by parts, it is possible to re-write Eq. 2.16:

$$n \neq \ell : c_\ell(t) = -\frac{W_{1,\ell n}}{\hbar \omega_{\ell n}} \left(f(T) e^{i\omega_{\ell n} T} - \int_0^T \frac{df(t)}{dt} e^{i\omega_{\ell n} t} dt \right) - \frac{W_{2,\ell n}}{\hbar \omega_{\ell n}} \left(\ddot{x}_0(T) e^{i\omega_{\ell n} T} - \int_0^T \frac{d\ddot{x}_0(t)}{dt} e^{i\omega_{\ell n} t} dt \right) \tag{2.17}$$

We can now explicity write out $\Psi(T)$ using Eq. 2.14 with coefficients $c_\ell(t)$ defined by Eq. 2.15 and Eq. 2.16.

$$\begin{aligned}\Psi(T) &= \Bigg[\Big(1-\frac{i}{\hbar}W_{1,nn}\int_0^T f(t)dt\Big)\Psi_n - \sum_{\ell\neq n}\Bigg(\frac{W_{1,\ell n}}{\hbar\omega_{\ell n}}\Big(f(T)e^{i\omega_{\ell n}T} - \int_0^T \frac{df(t)}{dt}e^{i\omega_{\ell n}t}dt\Big) \\ &+ \frac{W_{2,\ell n}}{\hbar\omega_{\ell n}}\Big(\ddot{x}_0(T)e^{i\omega_{\ell n}T} - \int_0^T \frac{d\ddot{x}_0(t)}{dt}e^{i\omega_{\ell n}t}dt\Big)\Bigg)\Bigg]e^{-i\omega_n T} \qquad (2.18)\end{aligned}$$

Using Eq. 2.12, it is possible to write out the final available states of the ion at the end of the perturbation:

$$\Psi_m^f = \Psi_m^i + \sum_{k\neq m}\frac{W_{1,km}f(T) + W_{2,km}\ddot{x}_0(T)}{\hbar\omega_{mk}}\Psi_k \qquad (2.19)$$

The transition amplitude between $\Psi(T)$ and Ψ_m^f is:

$$\begin{aligned}\langle\Psi(T)|\Psi_m^f\rangle &= \Big(1+\frac{i}{\hbar}W_{1,nn}\int_0^T f(t)dt\Big)\Big(\frac{W_{1,nm}f(T)+W_{2,nm}\ddot{x}_0(T)}{\hbar\omega_{mn}}\Big)e^{i\omega_{nn}T} \\ &- \frac{W_{1,nm}}{\hbar\omega_{mn}}\Big(f(T)e^{i\omega_{mn}T} - \int_0^T\frac{df(t)}{dt}e^{i\omega_{mn}t}dt\Big)e^{i\omega_{nn}T} \\ &- \frac{W_{2,nm}}{\hbar\omega_{mn}}\Big(\ddot{x}_0(T)e^{i\omega_{mn}T} - \int_0^T\frac{d\ddot{x}_0(t)}{dt}e^{i\omega_{mn}t}dt\Big)e^{i\omega_{nn}T} + O(W^2) \qquad (2.20)\end{aligned}$$

Recall that the shuttling process should not cause any transitions between the n-th eigenstate of the initial Hamiltonian in the position representation to the m-th eigenstate of the final Hamilitionian in the position representation (m≠n). One way to do this is to make the the following condition true:

$$\begin{aligned}f(T)e^{i\omega_{mn}T} &\gg \int_0^T\frac{df(t)}{dt}e^{i\omega_{mn}t}dt \qquad (2.21)\\ \ddot{x}_0(T)e^{i\omega_{mn}T} &\gg \int_0^T\frac{d\ddot{x}_0(t)}{dt}e^{i\omega_{mn}t}dt\end{aligned}$$

If the above conditions are true, it can be seen that there will be a first order cancellation of the transition amplitude in Eq. 2.20. One way to ensure that the

conditions in Eq. 2.21 are met is to follow the suggestions of Griffiths[28].

$$\left|f(t)W_{1,nm} + \ddot{x}_0 W_{2,mn}\right| \gg \left|\frac{W_{1,mn}\dot{f}}{\omega_{mn}} + \frac{W_{2,mn}}{\omega_{mn}}\frac{d\ddot{x}_0}{dt}\right| \tag{2.22}$$

To see why this makes Eq. 2.21 true, consider the ratio:

$$\frac{\int_0^T \partial_t f(t) e^{i\omega_{mn}t} dt}{f(T)e^{i\omega_{mn}t}} = \int_0^T \frac{\partial_t f(t)}{f(T)} e^{i\omega_{mn}(t-T)} dt \ll 1 \tag{2.23}$$

If the ratio of $\partial_t f(t)$ to $f(T)$ is nearly constant over the integral, then it can be pulled outside of the integral to a very good approximation. The remaining integral is an elementary integral of an exponential:

$$\frac{\partial_t f(t)}{i\omega_{mn} f(T)}\left(1 - e^{-i\omega_{mn}T}\right) \ll 1 \tag{2.24}$$

Since the magnitude of the exponential oscillates between zero and one, the only way to make Eq. 2.24 always true is to make the modulus of the fraction in Eq. 2.24 much less than unity.

An objection to this method for obtaining the adiabatic constraints in Eq. 2.21 or Eq. 2.22 is that the perturbation of the Hamiltonian may not in the perturbative regime and first order perturbation theory may not be valid. However, as pointed out by Griffiths [28], this derivation for the adiabatic condition holds for large perturbations W too. If the perturbations are large, the shuttling time T can be divided into N subintervals for which it is applicable to apply first order perturbation theory, particularly when writing out the wavefunction of the final Hamiltonian in terms of the initial Hamiltonian in Eq. 2.19. Since there are N total subintervals, the transition amplitude would be proportional to $N(W/N)$ which can be large if the perturbation is large. However, the transition amplitude is proportional to $N(W/N)^2 = W^2/N$ which tends to zero as N goes to infinity.

The adiabatic condition in Eq. 2.22 is not necessarily the only unique way to shuttle an ion adiabatically. The equation assumes that the change of the Hamiltonian is slow; there may be other methods of shuttling ions very quickly. For example, if

one had access to the phase of oscillation of the ion in the trap, it might be possible to translate the trap in such a way that the change in acceleration of the trap does not give energy to the ion. This is similar to the way a crane operator moves a heavy object. Near the end of the movement of the object, the crane operator decelerates and then speeds up again to match the oscillation of the object. The adiabatic condition in Eq. 2.22 may be the easiest to perform experimentally because it does not require any knowledge about the phase of oscillation of the ion or the details of how the ion is accelerating during its secular motion. The tradeoff is that the adiabatic condition in Eq. 2.22 may not yield the fastest shuttling time while preserving the number state of the ion. There are two important special cases to be illustrated using the adiabatic equation of constraint presented here. If the ion is not accelerated then $\ddot{x}_0(t) = 0$ and the condition on adibaticity is:

$$\omega_{mn} \gg \frac{\dot{f(t)}}{f(T)} \tag{2.25}$$

If the ion is shuttled with constant secular frequency, then $f(t) = 0$ making the adiabatic condition:

$$\omega_{mn} \gg \frac{1}{\ddot{x}_0(T)} \frac{d\ddot{x}_0(t)}{dt} \tag{2.26}$$

In both Eq. 2.25 and Eq. 2.26, there is a clear comparison of the internal time of the system (the period of oscillation) and the external time of the system (the change of the Hamiltonian). Both equations demand that the ion sweep out its phase space many times before the effective potential changes very much. Secondly, Eq. 2.26 says that if an ion is to be shuttled between two trapping zones as quickly as possible, then it is better to have a high secular frequency than a low secular frequency. Lastly, Eq. 2.26 specifies a design parameter with which to optimize a method of accelerating an ion. The optimal way to shuttle an ion with constant secular frequency is to minimize $\partial_t \ddot{x}_0(t)/\ddot{x}_0(T)$.

The appearance of a third derivative of $x_0(t)$ at first may seem suspect, but it

makes sense physically. An acceleration of the potential alone (with constant secular frequency) does not induce transitions in the number state of the ion because in the moving frame, the originally quadratic potential only experiences as deformation with constant accleration. However, if the acceleration is changing in time, the effective potential in the moving frame changes in time. This can induce transitions between the number states of the ion. The adiabatic condition only depends on the first derivative of the function $f(t)$ because if f changes in time, the effective potential in the frame of the ion changes as well.

Although the adiabatic transport of an ion in the context of quantum information is presented here, the derivation of the transport of matter in a harmonic oscillator potential is completely general and may be an important consideration in other atomic physics experiments where it is desirable to transport cold matter adiabatically in harmonic wells so that atoms are not excited out of their ground state.

2.3.2 Adiabatic Optimization

The ideal shuttling protocol keeps constant secular frequency and does not have a changing acceleration. The constant secular frequency keeps the energy level spacing from changing because the energy level spacing of a quantum harmonic oscillator is given by the secular frequency of the ion. Although it may seem like having a constant acceleration will give the ion more energy, a constant acceleration by itself does not induce transitions in the number state of the ion during a shuttling protocol. As can be seen in Eq. 2.11, a constant acceleration of the harmonic oscillator looks like a warping of the potential in the frame of the ion. A perturbed harmonic oscillator that is static in the frame of the ion does not induce transitions to other harmonic oscillator number states. However, a change in the acceleration of a harmonic well can induce transitions to other number states during the shuttling process.

The important question to ask about quickly shuttling ions between trapping

zones is as follows. Given a particular distance and a particular time in which to traverse the given distance, what is the best way to change the equilibrium position of the ion in the harmonic well so that the shuttling process gives a minium probability of transition to other number states during the shuttling process.

Clearly via equation 2.22, one good way to do this is to shuttle the ion with constant secular frequency and to translate the potential with constant velocity. This of course should correspond to no change in the ion's state because physics is not sensitive to constant velocity and an unchanging secular frequency means that the energy levels are not being perturbed. There may be other ways to do this as well, such as to implement some kind of complicated simultaneous change in the acceleration of the ion and its secular frequency in order to optimize the adiabatic approximation. There may be even better ways to adiabatically shuttle if the phase of oscillation of the ion is known and an appreciable change in the equilibrium position of the ion can take place on the timescale of the period of oscillation of the ion's motion.

A question arises about the adiabaticity at the beginning and end of the shuttling procedure with constant linear velocity because it is necessary to start moving and to stop moving at the end of the shuttling protocol. In other words, there is a discontinuity in the velocity of the ion and hence the acceleration diverges at these start and stop points. In a real world ion trap system, it is impossible to change the voltages on the electrodes infinitely fast to kick the ion infinitely fast because there must be some sort of low pass filter element in the circuit. In fact, low pass filters are typically implemented to filter out RF noise from the RF electrodes. In other words, there are no difficulties with infinities arising from stopping and starting the shuttling process. However, a sudden commencement and finish of the shuttling protocol with constant velocity shuttling in between can cause transitions and in general depends on the details of the characteristic RC time constant of the electrical system that connects up the electrodes. However, neglecting the problems with starting and stopping the ion, shuttling

the ion with constant velocity is clearly the most adiabatic way to shuttle because there is no pertubration of the Hamiltonian.

2.3.3 Transition Probabilities of Real Shuttling Protocols

No real world shuttling protocol will ever be perfectly adiabatic, so it is interesting to look at what the transition probabilities are for non-ideal shuttling. In other words, by not imposing the restrictions from Eq. 2.21, the remaining first order transition amplitude is:

$$\langle \Psi(T)|\Psi_m^f\rangle = e^{i\omega_n t}\left(\frac{W_{1,mn}}{\hbar\omega_{mn}}\int_0^T \partial_t f(t)e^{i\omega_{mn}t}dt + \frac{W_{2,mn}}{\hbar\omega_{mn}}\int_0^T \ddot{x}_0(t)e^{i\omega_{mn}t}dt\right) \quad (2.27)$$

The probability of a transition between the different number states is the modulus squared of the above equation. There are several features to note about the above equation as well. The first is the selection rule of the transition. The static parts of the perturbation ($W_{1,mn}$ and $W_{2,mn}$) allow for dipole and quadrupole transitions. The scaling of the perturbations is interesting as well. Almost every factor in the first term of Eq. 2.27 cancels, but when the integral is performed, the transition amplitude will be proportional to the area under the $f(t)$ term from $t = 0$ to $t = T$ and will be inversely proportional to the difference between ω_m and ω_n. In other words, the tighter the trap is, the less sensitive the ion will be to undergoing transitions due to a modulated potential well curvature. The second term is inversely proportional to ω_0 to the 3/2 power, so again, shuttling is more adiabatic with a higher secular frequency. Integration of the second term makes the transition amplitude inversely proportional to $\omega_m - \omega_n$. The second term also scales linearly in the acceleration of the harmonic well, so minimizing the acceleration is important. The second term is also proportional to the square root of the mass of the ion, so for a fixed shuttling protocol, shuttling is more adiabatic with a lighter ion!

Chapter 3

Experimental Apparatus

3.1 T-trap Design

3.1.1 T-junction Ion Trap Array Design

The purpose of building and testing the T-junction ion trap array was to perform a proof of principle experiment toward the vision of Kielpinski et al[2] where ions could be arbitrarily shuttled throughout a two dimensional ion trap array. The T-trap consists of two, three-layer linear traps that are joined at a 90 degree angle (see Fig. 3.1, 3.2). There are 11 trapping zones in the T-trap as can be seen in Fig. 3.1 numbered a-k. The number of trapping zones was chosen so that if an ion is confined in zone k, other ions can be shuttled from zone a and zone h greatly perturbing in the trapping potential in zone k.

There are 48 control electrodes in the T-junction ion trap as indicated in Fig. 3.1 of which 28 are not grounded and are used to shuttle ions. The non-grounded control electrodes have a width of 400 μm away from the junction region, but are much wider ($\sim$800-900 μm) around the junction. The larger electrodes are not ideal for precisely controlling the potential near the junction region; smaller electrodes near the junction region are desirable so that the motion of the ion can be more precisely controlled in the junction region. The channels are 200 μm wide and the bottom to top layer separation is also 200 μm. The RF layer in the center is a single, non-segmented electrode to ensure

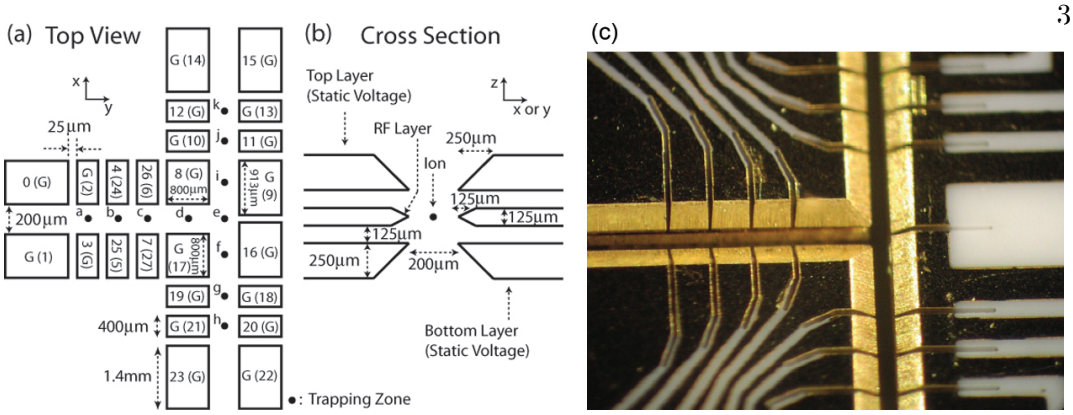

Figure 3.1: T-junction ion trap array schematic. This 11-zone, three layer T-junction ion trap has 48 control electrodes of which 28 are non-grounded and a central RF layer. Fig. 3.1a shows a top view of the T-trap. The 11 trapping zones are indicated with letters a-k. The control electrodes are numbered with G indicating a grounded electrode. The parantheses indicate the bottom layer. Fig. 3.1b shows a cross section view of the T-trap looking down a channel. The top and bottom layers are consist of segmented control electrodes that are used to trap ions and shuttle them. The central RF layer confines the ions in the xy plane. Fig 3.1c shows the top layer of the actual T-junction ion trap.

that the phase and voltage of the RF is approximately the same everywhere in the trap.

Alumina substrates were laser machined to have a T-junction cut in them. The segmented control electrodes (top and bottom layers in Fig. 3.1 b) were made using wet chemical etching and dry-film photolithography techniques by first depositing 0.015 μm thick titanium tracks on the two outer alumina substrates, followed by a 0.4 μm thick layer of gold on the titanium. The non-segmented central RF layer was coated with a layer of gold by using an electron beam evaporator, and the three layers are pressed together by mount bars and are separated by 125 μm thick alumina spacers.

The electrodes are wire bonded to a gold bond pads that coat a quartz plate (see Fig. 3.2). The quartz plate also has chip resistors and capacitors that are wire bonded to more gold bond pads; the circuit is arranged to form a single pole, low pass RC circuit with RC = 1 μs (R = 1 kΩ, C = 1 nF) for each non-grounded control electrode. The low-pass RC filters are needed to filter noise that is near the secular frequency of a trapped ion (usually a few MHz) so that the noise can not resonantly drive the ion's

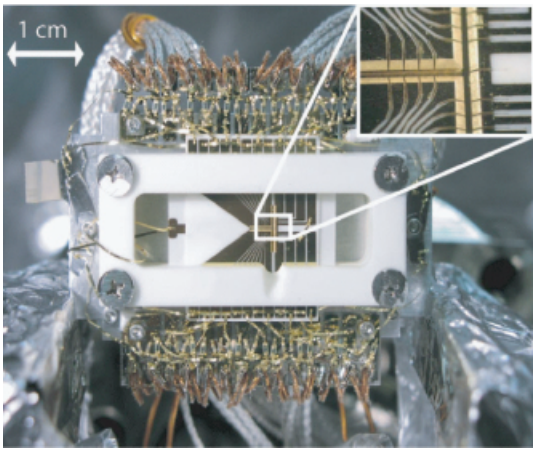

Figure 3.2: T-junction ion trap array with associated wires. The three layers of the T-junction ion trap are held together with alumina mount bars, and alumina spacers separate the three layers. The chip capacitors are visible near the top and bottom of the quartz plate near the top and bottom of figure.

motion. The assembled and mounted trap array before it was mounted in the vacuum chamber is shown in Fig. 3.2.

As can be seen in Fig. 3.2, the wiring of the T-trap is quite complex. There are wire bonds that connect each eletrode to its own low-pass RC filter. The RC filter elements are wire bonded to gold on a quartz substrate and are wired to each other with wire bonds. The vacuum leads that supply voltage to the T-trap control electrodes are all wire bonded to the RC filters. Wire bonds connect the RF ground of all of the RC circuits together. In all, there were over 2000 wire bonds necessary to hook up 28 out of the 48 control electrodes and to ground the remaining electrodes as well as provide RF filtering. If a trapped ion system is to be built with hundreds thousands of trapped ions, it is necessary to take the physical wiring of the system in to consideration. It will become necessary to integrate filtering circuits and wiring directly on the substrate, and it will also become necessary to have a chip carrier so that ion traps may be "plugged" in to a vaccum system to prevent the need for manual wiring. Lastly, it may be necessary to have a vacuum electronics board that has one end in vacuum and one end out of vacuum so that the circuit can be modified externally.

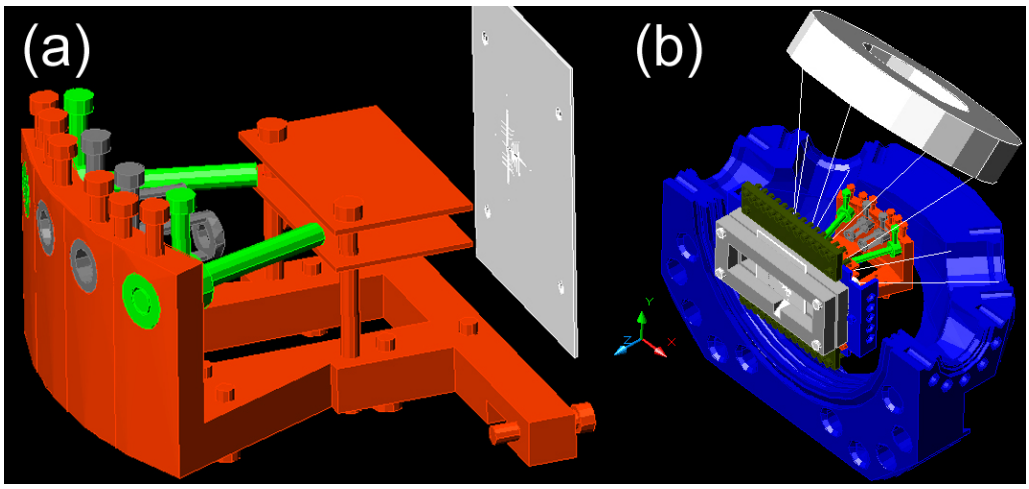

Figure 3.3: CAD drawing of T trap mounting range and hemispherical vacuum setup. Fig. a shows the relationship of the cadmium ovens (green), electron guns (grey), and mounting range (orange) to the alumina substrate where the T-junction electrodes are deposited (light grey slab). There are two cadmium flux mask planes mounted orthogonal to the alumina substrate that are designed to limit the exposure of the electrodes to direct cadmium flux from the ovens as well as aid in the acceleraton of electrons from the electron guns. Fig. b shows how the T-trap is mounted in a hemispherical vacuum chamber and shows the optical access to the T-trap through windows on both the sides and near the top of the chamber as depicted by white lines. The large viewport is screwed on the the vaccum chamber on the flat side of the chamber in Fig. b. Scattered light from the ions is collected through this veiwport.

3.1.2 Vacuum Design

The T-trap is mounted in a hemispherical vacuum chamber near a large fused silica viewport that is parallel the plane of the T-trap. There is optical axis through the large viewport window as well as two windows that are at a ∼54 degree angle relative to the normal direction of the large viewport window. These windows give optical axis to the stem of the T-junction where ions are primarily loaded. There is also another viewport that is tipped up to allow for optical axis into the top of the T. A drawing of the mounted T-trap inside a vaccum hemisphere can be seen in Fig. 3.3a,b. In Fig. 3.3a, the relationship of the ovens (green), electron guns (gray), and mounting range (orange) to the T-trap can be seen. Cadmium ovens reside in the chamber and point toward the stem of the T much like a musket. Tungesten wire is wrapped around the

oven and current is run through the wire to heat cadmium oxide in the oven. In order to wrap the tungensten wire around the ceramic tube, it is useful to first wrap the wire through a screw and then twist the wire off of the screw. The ceramic tube can then be inserted in the center of the wire wrapping. The bottom of the tube is filled with ceramic paste to prevent cadmium from falling toward the mounting range where the temperature is much lower. After packing the tube ∼1cm with cadmium oxide, it is helpful to glue an aperture over the opening of the tube. After the oven is fired for the first time, the remaining cadmium in the tube will become a solid pellet instead of a powder, and the pellet will be too wide to pass through the aperture.

The cadmium ovens contain a brownish-red cadmium oxide powder. The ovens are tested under vacuum ($\sim 10^{-6}$ Torr) in a bell jar where cadmium flux is measured using a residual gas analzyer. After such tests, the brownish-red cadmium oxide powder becomes a solid grey pellet, suggesting that heating cadmium oxide under vacuum can remove the oxygen atoms to leave solid cadmium in the ovens. A measured cadmium partial pressure of 10^{-10} to 10^{-9} Torr in the bell jar is sufficient amount of cadmium flux to load ions in an ion trap. It is actually possible to forgo ovens in a cadmium system because the partial pressure of cadmium at room temperature is approximately 10^{-11} Torr in our vacuum systems. This is approximately equal to the background pressure needed for trapping. It is possible to simply place a small piece of cadmium in the vacuum chamber and use a pulsed laser to ionize the background vapor of cadmium in the trapping region. The non-use of cadmium ovens may decrease the amount of cadmium coating on the gold trap electrodes. This coating process may contribute to the observed anamolous heating of trapped ions [29],[30],[31].

Fig. 3.3b shows the T-trap mounted inside a hemisphere vacuum chamber. The white mount bars clearly visible in Fig. 3.2 are grey rectangles. The dark green quartz plate is has all of the wire bonds attached to it near the top and bottom of Fig. 3.2. The T-trap is mounted sideways in Fig 3.3 so that the stem of the T is horizontally oriented

and the top of the T is oriented vertically. The hemispherical chamber is designed so there is optical access to the stem of the trap through two small windows on the side of the chamber. The optical access to the top of the T is provided by the larger window shown in Fig 3.3. The white lines in the figure show the region of the vacuum where there is optical access.

A 50-pin feedthrough was used to connect all of the wires that come off of the T-trap as can be seen in Fig. 3.2. It is tempting to use wire with extra metal insulation around the insulator to provied better shielding as is shown in Fig. 3.2, but this should be avoided at all costs. When pushing the vacuum feedthrough onto the vacuum chamber, the loose metal insulation will be pushed up the kapton wire and could short or break wire bonds.

3.1.3 Electronics

It is necessary to have high-voltage, fast, low noise amplifiers to control the trapping potential of the ions and to shuttle them using control electrodes. In order to shuttle ions around the corner in the T-junction, it was necessary to be able to change the output of the amplifiers by 10 volts in 1 μs. This was accomplised using PA85A amplifiers from Apex. This op-amp was chosen specifically because the amplifier has an output voltage range of 450 Volts, a high slew rate of 1 kV/μs and a measured voltage noise of less than 3 $\mu\mathrm{V}/\sqrt{Hz}$. The circuit diagram is in Fig. 3.4. There are several design parameters to consider when picking resistance values for the amplifier circuit. In order to limit the current output, the value of R_{CL} may be adjusted according to the following equation:

$$R_{CL}(\Omega) = \frac{0.7}{I_{max}/(A) - 0.016} \tag{3.1}$$

We chose to limit the current to 40 mA.

In order to change the voltages on the control electrodes as quickly as possible, the circuit was optimized to give the fastest voltage swtiching time for a given voltage

gain. Because the computer controlled analog output card is limited from +10V to -10V, an op-amp gain of ∼30 was chosen. The original resistance values of R_1 and R_2 were 56 kΩ and 1.56 MΩ respectively. The large resistance values were chosen so that there would be little current flow through the resistors to place as little strain on the op-amps as possible. These large resistance values slowed down the slew rate of the op-amps, so the values of R_1 and R_2 were changed to 12 kΩ and 400 kΩ respectively. This change offered nearly a factor of 10 speed up in the voltage switching time.

The op-amp circuit has a frequency response that resembles a low pass RC filter with a 3dB point at ∼ 125 kHz which gives an effective RC time constant of 8 μs. Since this time constant is about 8 times larger than the RC filtering circuit next to ion ion trap array on the quartz plate, the frequency response of the op amp circuit is the dominant factor in determining the frequency response of the system.

The amplifying circuit used in the T-trap is shown in Fig. 3.4 is used to amplify the voltages from the output of computer controlled analog voltage output cards (National Instruments 6733). The noise from the analog output card and the noise from the amplifying circuit is less than 3 $\mu V/\sqrt{Hz}$. The analog voltage output voltages in discrete time steps and can be programmed with LabView software. Because the output of the voltage card is discrete in time, the potential in the ion trap can change abruptly if the voltage card puts out voltages at a rate that is much slower than the RC time constant of the trap filters and op-amp circuit. The voltage cards are able to output a new voltage every μs, so the the op-amp frequency response smooths out any voltage steps.

3.2 Photoionization of Neutral Cadmium

In order to trap cadmium ions in an ion trap, neutral cadmium atoms are ionized by removing the a 5s electron to give a singly ionized Cd^+ ion with a single s-shell electron. The electron can be removed via electron impact ionization or with photoion-

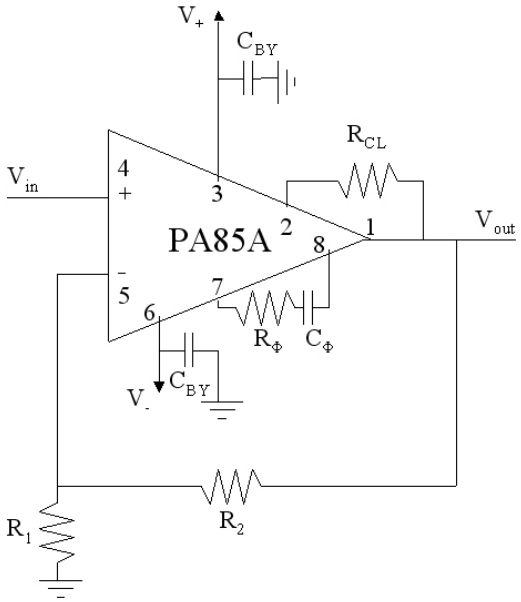

Figure 3.4: The value of R_1 is 12 kΩ and R_2 = 400 kΩ so that the gain is approximately 34.3. The capacitor C_{BY} filters the input power supply so that fast (of order MHz) noise from the power supply noise does not interfere with trapping if the amplifier is run near rail and has a value of 10 μF. The series RC circuit consisting of R_ϕ and C_ϕ compensate for phase differences during amplification of time-dependent voltages and have values of 220 Ω and 10 pF respectively. The resistor R_{CL} limits the current output of the amplifier as descirbed by Eq. 3.1. The current was limited to 40 mA by selecting R_{CL} = 30 Ω.

ization. With electron impact ionization, a neutral cadmium gas is bombarded with $\sim$200 eV electrons. The disadvantage of using this method is that the electrons can charge up dielectric surfaces near the trap and alter the electric field in the ion trap potentially creating difficulties with trapping ions.

Photionization of cadmium is a clean way to remove the outer electron from cadmium. A mode-locked Ti:Sapphire pulsed laser is frequency quadrupled to produce $\sim$5-10 mW of average power at 228.8 nm and focused down to a $\sim$ 15μm waist to photoionize neutral cadmium in a two photon process. One photon promotes a 5s $^1S_0$ electron to the 5p $^1P_1$ level. A second photon then takes the $^1P_1$ population into the continuum by $\sim$3.6 eV. The pusle duration of the laser is of order 1 ps, so the bandwidth of the laser is $\sim$10nm. The large bandwidth of the laser will photoionize all velocity

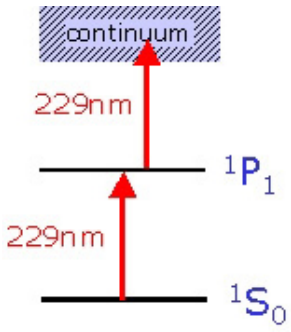

Figure 3.5: Photoionization process for neutral cadmium. A frequency quadrupled mode-locked Ti:Sapphire laser excites the 5s $^1S_0$ electron to the 5p $^1P_1$ level which is then excited to the continuum by a second photon at 228.8 nm. The bandwidth of the pulsed laser is large enough to photoionize all velocity classes of atoms.

classes of neutral cadmium atoms in the trapping region. Although isotope selectivity is not obtained with a pulsed laser, the loading rate is about 0.1-1 ion per second, so effective isotope selectivity can be obtained by dumping the trap and loading a different ion[32].

Ions are loaded into the trap by applying $\sim$ 400V RF at $\omega/2\pi \sim 48$ MHz, 17V to confine the ion in the x direction, and -3V to the electrodes nearest the trapping zone. Cadmium oxide ovens are heated to supply cadmium vapor, although loading of ions is still possible without running the ovens due to the vapor pressure of cadmium at room pressure and at ultra-high vacuum pressures inside the vacuum chamber[32].

3.3 Laser Cooling and Detection

Singly ionized $^{111}Cd^+$ has a single valence shell electron and a spin 1/2 nucleus and thus have a hydrogen-like energy level structure (see Fig. 3.6). The ground state of both species is split into singlet and triplet hyperfine states by the spin-spin coupling of the nuclear magnetic moment to the valence shell electron's magnetic moment. Unlike hydrogen, the nuclear magnetic moment of cadmium is negative, so the triplet state is lower in energy than singlet state. Singly ionized cadmium also has a much larger hyperfine splitting (14.5 GHz) than hydrogen (1.42 GHz). The energy levels of cadmium

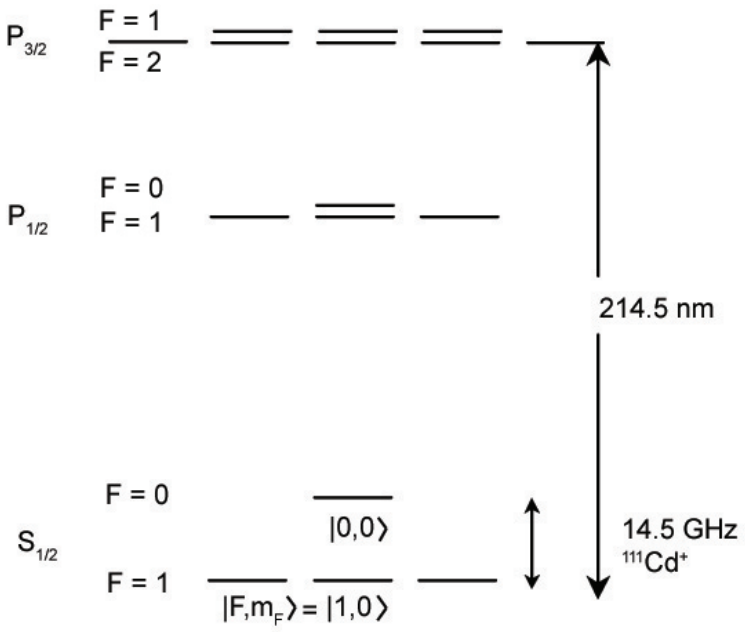

Figure 3.6: $^{111}Cd^{+}$ energy level structure. The $^{111}Cd^{+}$ level structure is similar to atomic hydrogen because both species have a single valence electron. The $^{111}Cd^{+}$ hyperfine structure is large compared to the linewidths of the S and P manifold energy levels. The large hyperfine structure of the $^{1}S_{1/2}$ ground state allows for good detection efficiency between the $|F, m_f\rangle = |1, 0\rangle$ and the $|0, 0\rangle$ state using the a laser that is resonant with the $S_{1/2}$ F=1 manifold and the $P_{3/2}$ manifold.

are typically expressed in the $|F, m_F\rangle$ basis where $F = J + I$ is a sum of the valence electron's spin and orbital angular momentum and the spin angular momentum of the nucleus.

The $|F, m_F\rangle = |1, 0\rangle$ and $|0, 0\rangle$ hyperfine states of odd isotopes of cadmium ($^{111}Cd^{+}$, $^{113}Cd^{+}$) are the $|0\rangle$ and $|1\rangle$ qubit states. Either state can easily be prepared using standard optical pumping techniques[33]. The $|0, 0\rangle$ state can be prepared using a π- polarized laser tuned the $S_{1/2}$ F $= 1 \rightarrow P_{3/2}$ F $= 1$ transition. The most probable decay channel is from $P_{3/2}$ F $= 1 \rightarrow S_{1/2}$ F $= 0$, so all of the population eventually ends up in the $S_{1/2}|0, 0\rangle$ state. The $S_{1/2}$ $|1, 0\rangle$ state can be prepared by first intializing to the $S_{1/2}|0, 0\rangle$ state and then performing a microwave transition. The hyperfine states of cadmium are attractive candidates for qubits because they are insensitive to mag-

netic fields to first order ($m_F = 0$) and the hyperfine splitting is much larger than the linewidths of any of the $P_{3/2}$ states, so it is possible to efficiently detect either qubit state. The ground state of cadmium has a large hyperfine splitting of 14.5 GHz which is much greater than the natural linewidths of the hyperfine states or the 800 MHz hyperfine splitting of the $P_{3/2}$ level. The large hyperfine splitting makes it easy to detect the $|F, m_F\rangle = |0, 0\rangle$ and the $|F, m_F\rangle = |1, 0\rangle$ level because the $|1, 0\rangle$ level can be tuned to the $S_{1/2} \rightarrow P_{3/2}F = 2$ transition while the $|0, 0\rangle \rightarrow P_{3/2}F = 2$ is too far off resonance to couple to the $P_{3/2}$ manifold.

The photon scattering rate γ_s of a trapped ion is given by the following Lorentzian [34]:

$$\gamma_s = \frac{s_0\gamma/2}{1 + s_0 + (2(\Delta + \omega_D)/\gamma)^2} \tag{3.2}$$

where γ is the excited state linewidth ($\sim 2\pi$ x 60 MHz for $^{111}Cd^+$), Δ is the detuning from the resonant transition, $s_0 = I/I_{sat}$ is the ratio of the laser intensity to the saturation intensity. The saturation intensity is related to the natural linewidth of the excited state and the wavelength:

$$I_{sat} = \frac{\pi\gamma hc}{3\lambda^3} \tag{3.3}$$

The other term in the denominator of Eq. 3.2 (ω_D)is the doppler shift as seen by the moving atoms in the path of the laser: $\omega_D = -\vec{k} \cdot \vec{v}$. The minus sign gives a positive doppler shift if the ions' velocity is opposite of the k-vector of the laser beam. The force on the ions is given by the time derivative of the expectation value of the momentum operator [34].

$$\vec{F} = \hbar\vec{k}\gamma_p \tag{3.4}$$

Ion's are slowed when $\Delta + \omega_D \ll \gamma$, and the force on the ions due to the laser saturates at large s_0 to $F_{max} = \hbar k\gamma/2$. If the ion is moving toward a laser that is red detuned from the resonant transition ($\vec{k} \cdot \vec{v} < 0$), the ions will scatter more light because in the frame of the ion, the light will appear closer to resonance. If the ion is moving away

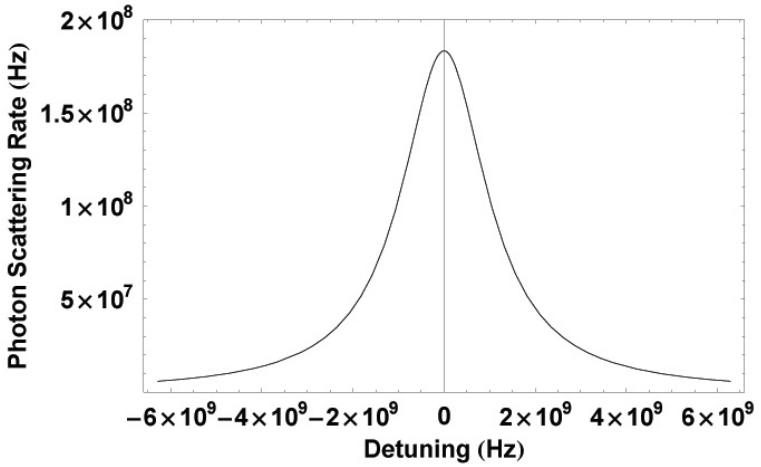

Figure 3.7: Photon scattering rate near $S_{1/2} \rightarrow P_{3/2}$ as function of detuning for typical laser parameters. The detection laser at 214.5nm with a power of 300 μW is focused down to a 15μm waist. The cadmium ion scatters approximately 75 million photons per second when the resonant laser is detuned about one linewidth red of of the $S_{1/2} \rightarrow P_{3/2}$ resonance.

from a red-detuned laser ($\vec{k} \cdot \vec{v} > 0$), the ions will scatter less light because in the frame of the ion, the light appears to be further from resonance. The overall imbalance of the photon scattering rate makes ions slow down more when they are moving into the k-vector of the laser because the ions scatter more photons. Counter-propagating beams are not needed in ion traps because the restoring force of the trap will allow the ion to lose kinetic energy when the phase of the ion's oscillation is such that $\vec{k} \cdot \vec{v} < 0$.

Dectection of a trapped and cooled ion is done by imaging the scattered photons from the ion. Light that is σ^+-polarized and tuned to the $S_{1/2} \rightarrow P_{3/2}$ transition optically pumps the ion into the $S_{1/2}|1,1\rangle$ state. The cycling transition between the $S_{1/2}|1,1\rangle$ state and the $S_{3/2}|2,2\rangle$ scatters ~75 million photons per second for a detuning of -200 MHz from resonance.

The detection wavelength of 214.5 nm is generated by using a 10 W Nd-YAG pump laser to pump a Ti:Sapphire laser to produce ~1.5 W of light at 858 nm. This infrared laser is frequency doubled with an LBO crystal inside of a cavity to yield 300 mW of light at 429 nm. The resulting blue light is then frequency doubled a second

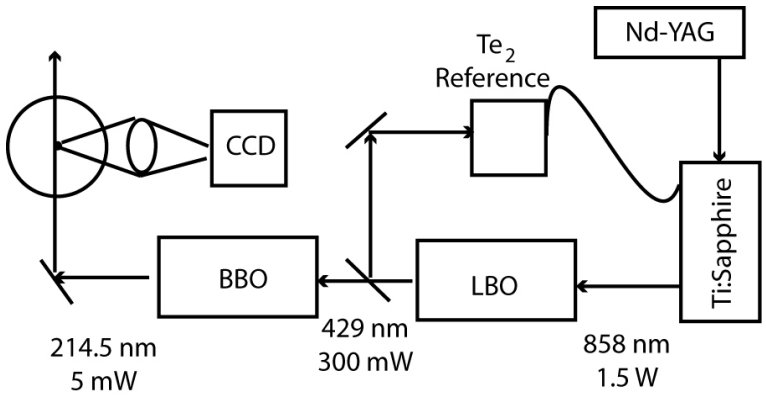

Figure 3.8: A 10.5 W Nd-YAG laser pumps a Ti:sapphire laser to produce 1.5 W of light with wavelength of 858nm. This light is frequency doubled in an LBO cavity to give 300 mW of light at 429 nm. Part of this light is picked off and directed to a Te_2 reference cell to feed back into the cavity of the Ti:Sapphire laser. The rest of the light at 429 nm is frequency doubled in a BBO cavity to give the radiation necessary for cooling and detecting ions in an ion trap. The scattered photons are imaged on a CCD camera.

time with a BBO cavity inside of a cavity to yield ∼5mW of UV light at 214.5 nm. The laser set up is shown in Fig. 3.8. The scattered photons are collected by f/2.1 optics and imaged on a CCD camera. The image is magnified so that a 550 x 550 μm area can be seen in the trap so that ions can simultaneously be imaged in zone d and zone i or f. The nearly diffraction limited ion appears to be a bright spot that is a few pixels wide on the CCD camera.

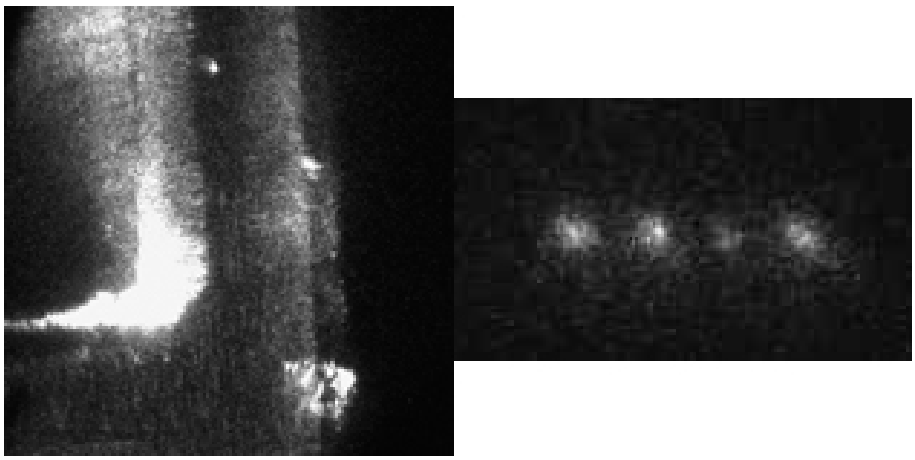

Figure 3.9: Trapped ions imaged with a CCD camera. The picture on the left shows an ion trapped in zone f in the T-junction ion trap array. A corner electrode is plainly visible. The picture on the right shows a chain of four trapped ions. The third ion from the left is a different isotope of cadmium so the $S_{1/2} \rightarrow P_{3/2}$ transition is at a different wavelength and the ion scatters fewer photons than the other three ions near their $S_{1/2} \rightarrow P_{3/2}$ transition.

Chapter 4

Surface Electrode Chemistry

The trapping potential of ion traps is highly harmonic, so the treatment of the quantum states of the ions is that of the quantum harmonic oscillator. Gates that could be used for quantum computing schemes involve entangling the Coulomb-coupled motional states of ions to their electronic states[35],[36],[37].

There is an observed anomalous heating rate of the quantum state of motion of the ions in ion traps that causes decoherence [38],[39],[40]. The heating mechanism is from noisy electric potentials on trap surfaces that scales with the distance of the trapped ion to the nearest electrode $z^{-3.47\pm0.16}$ and is nonlinear in the temperature of the trap electrodes[41]. The electrical noise is theorized to come about from fluctating patch potentials near the trap secular frequencies that resonantly drive the ions' secular motion.

Anomolous heating above the Johnson noise limit has been observed in many ion trap systems and appears to become worse as the trap electrodes are coated with neutral atoms [39]. Curiously, most trap electrodes are gold and beryllium [42], barium [43], mercury [44], cadmium [45], calcium [46], and ytterbium [47] all form alloys with gold. Although the melting points of all of these materials is much higher melting points than will be experienced in typical ion trap experiments, the melting points of these materials may be significantly lower under high vacuum. At least two of these elements tend to stick to gold (cadmium and beryllium [39]) which may make it difficult to keep

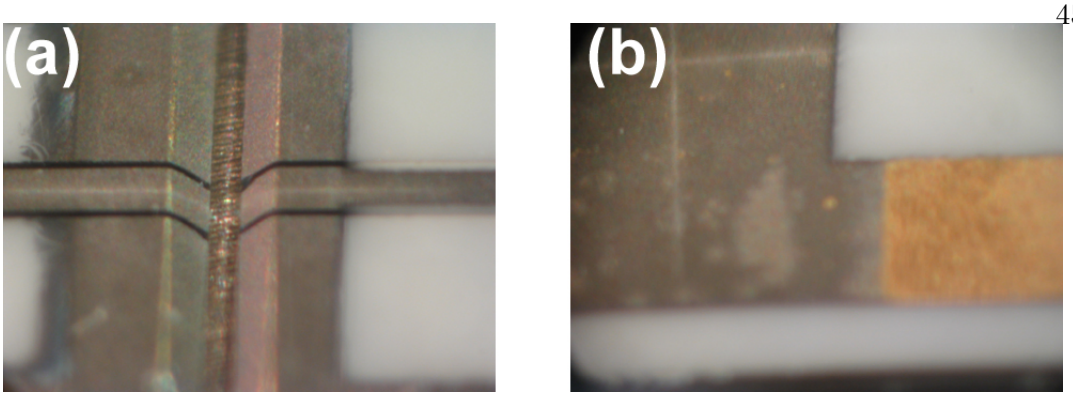

Figure 4.1: Gold electrodes coated and not coated with cadmium. Fig. fig:cdelectrodea is from one layer from a three-layer, one zone linear trap that was heavily used. The gold trap electrodes appear yellow because they are coated with cadmium. Fig. 4.1b is part of the same trap but part of a gold track that was partially shielded from cadmium oven flux. There is a sharp division between coated and uncoated gold.

the electrodes clean during vacuum bake outs and firing ovens to provide atomic flux to load an ion trap.

4.1 Atomic Force Microscopy Examination of Trap Electrodes

Significant cadmium deposition on gold trap electrodes results from operation of cadmium ovens and possibly from the 200^0C bakeout of the trap. The gold electrodes become coated with cadmium as can be seen in Fig. 4.1. These electrodes were bombarded with ∼100eV electrons, exposed to 214.5 nm radiation with an intensity of order 10^3 W/cm^2, baked at 200^0C while under vacuum as low as 10^{-12} Torr while being exposed to a neutral cadmium flux and background cadmium vapor. These environmental conditions made the gold electrodes turn to a dull grey color as they were coated with cadmium. In Fig. 4.1a, the top layer of a three-layer linear trap that has been heavily used in experiment is shown. The electrodes are no longer a bright, golden yellow color because cadmium has coated them to make them appear grey. Fig. 4.1b shows a gold track away from the trap electrodes that was partially shielded from cadmium flux. There is a sharp division between the area that is cadmium coated and the area that is

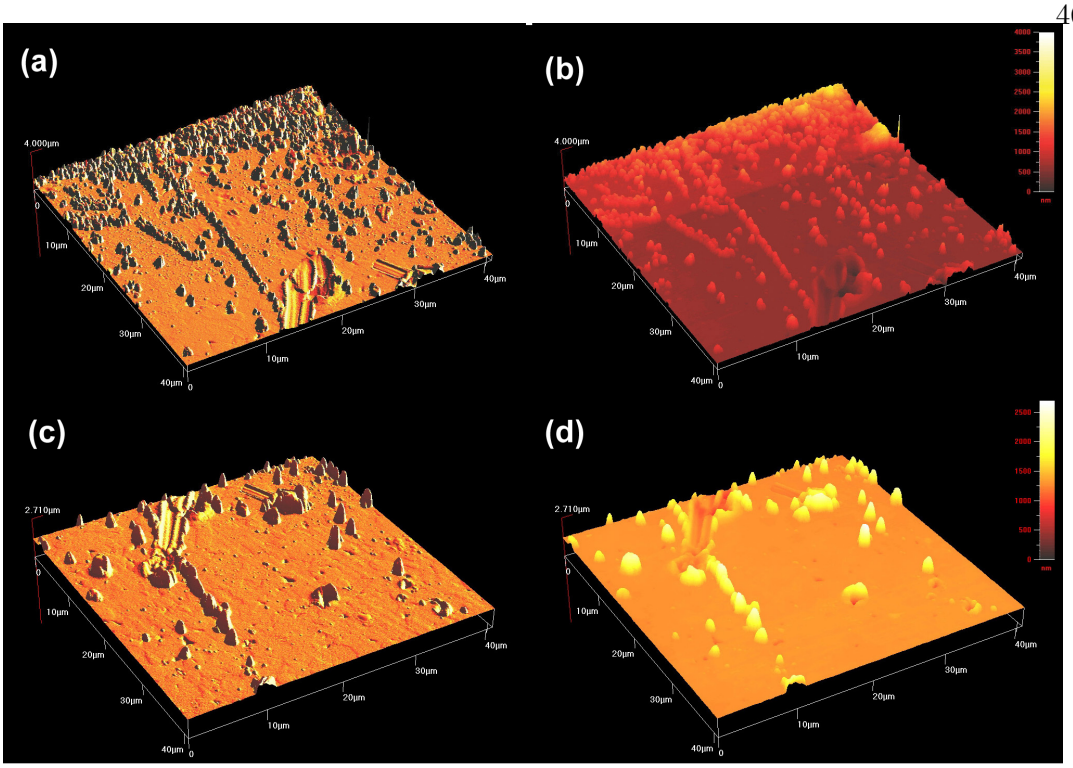

Figure 4.2: Gold cadmium boundary near a shielded electrode. The above figure shows the region where the gold (flat in the AFM scans) becomes heavily coated with cadmium (bumpy). Fig. 4.2a,b show slightly closer to the Au-Cd boundary than fig:afmaucdboundaryc,d. The bottom of 4.2a extends in to the top of 4.2c as can be seen from the large scratch in the gold in both AFM scans.

not cadmium coated.

These areas were examined using a Quesant Q-350 atomic force microscope in order to see if there is any macroscopic structure to the cadmium coating. In order to measure a lower bound on the thickness of the cadmium coating, the gold cadmium boundary in Fig. 4.1b was found. The atomic force microscope scan is in Fig. 4.2a-d. Fig. 4.2b shows that the cadmium coating is at least 4 μm thick near the gold-cadmium boundary shown in Fig. 4.1b. The gold itself is very flat as can be seen in Fig. 4.2c,d. AFM scans of the beveled side and top of the smallest middle electrode segment seen in Fig. 4.1a can be seen in Fig. 4.3a,b. The small electrode is closest to the center of the one zone linear trap from which this electrode layer was taken. There is a characteristic

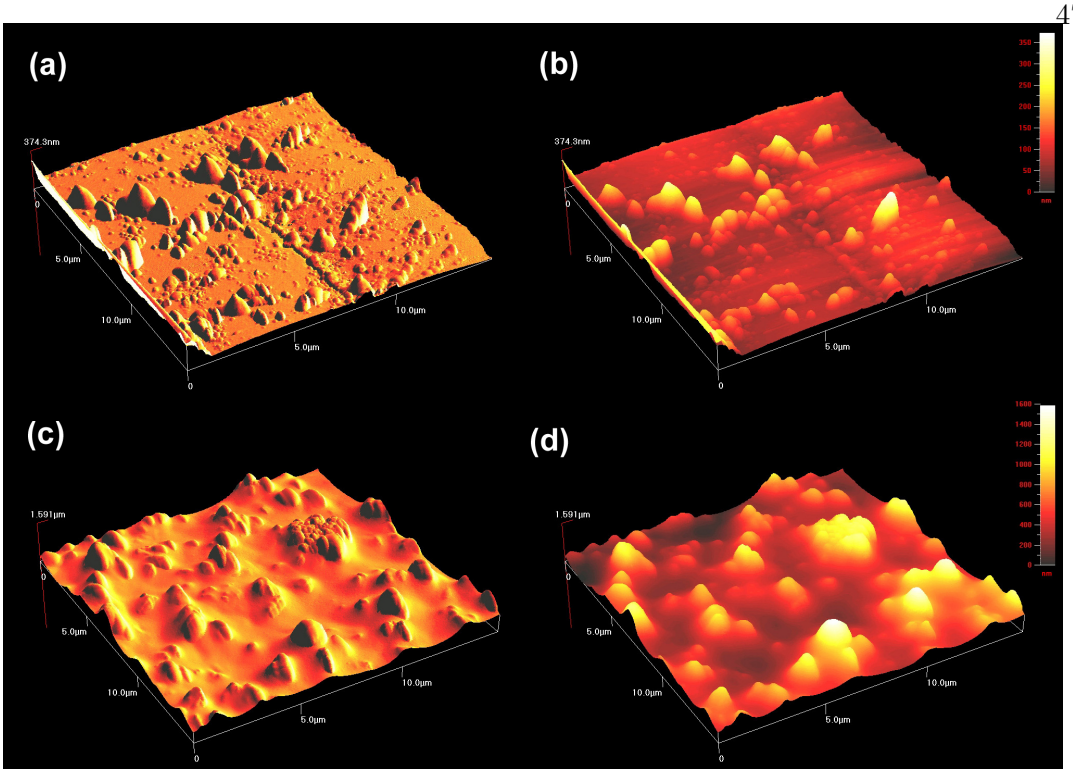

Figure 4.3: AFM scan of ion trap electrodes. Fig. 4.3a,b are scans of the beveled face of the cadmium-coated center electrope in Fig. 4.1a and have much smaller cadmium bumps than Fig. fig:afmtrapelectrodesc,d. The AFM scans in Fig. fig:afmtrapelectrodesc,d are from the top of the center, cadmium coated electrode in Fig. 4.1a.

bump size of 0.7 - 1.7 μm in the xy-plane of the scan and only 0.2 - 0.4 μm in height. The surfaces of these electrodes were most likely to be hit with the detection laser on a day to day basis. AFM scans were also taken of the top (non-beveled surface) of the center trapping electrode seen in 4.1b and are shown in Fig. 4.3c,d. The characteristic cadmium bump size is 1.4 - 2.2 μm in the xy-plane and 0.8 - 1.2 μm tall. These cadmium clumps are about 4 times as tall as the cadmium clumps on the beveled sides of the trap electrodes. The explanation for this may be that cadmium is laser ablated off of the trap electrodes, and since the beveled edge is more likely to be hit by the detection layer and (ionization laser in other traps), more cadmium should be removed from the in this region than on the top of the trap electrode. It should be noted that when the

detection laser or ionization laser is incident on the electrodes, the time it takes to load an ion decreases [32].

Chapter 5

Experimental Results

5.1 Classical Shuttling Protocols

If the vision of Kielpinski et al [2] is to be realized, it is necessary to have full, two dimensional control of ion shuttling so that any two arbitrary ions may be brought next to each other to be entangled in interaction zones. Linear shuttling alone is not enough because ions need to be sorted in an arbitrary order so that any two can be brough next to each other. Secondly, since ions need to be brought next to each other in the same trapping zone and then separated, there needs to be a way to separate ions that are in the same trap so that they may be shuttled to different trapping zones. There also needs to be a way to bring ions that are initially in different trapping zones together so that they are both in the same trapping zone.

In a two-dimensional array of ion traps, it is necessary to experimentally perform the following operations before a scalable two-dimensional geometry that relies on ion shuttling can be claimed:

(1) Linearly shuttling ions through channels and junctions

(2) Shuttling ions around corners

(3) Separating ions in the same trapping zone and combining ions into the same trapping zone

The goal of the T-junction ion trap experiment was to experimentally demonstrate all of these protocols as a proof of principle experiment for quantum computing schemes that involve the use of shuttling operations. However, at the time of the writing of this thesis, the DiVincenzo requirements for quantum computing have not been demonstrated in the T-trap.

5.2 Linear Shuttling

Linearly shuttling ions in linear Paul traps has been widely demonstrated by the NIST group ([48], [49], [10], [11]) and others [16]. Linear shuttling in the T-trap has proven very robust in the sense that the ion is not lost. The success rate of linearly shuttling ions between adjacent trapping zones ($\sim 400\mu$m) is greater than 99.9% even when the ions are shuttled in only 20μs.

Linearly shuttling across the junction of the T-trap has also been carried out with an efficiency of $\sim 98\%$, however, the total shuttling time required required to have this kind of efficiency is of order 10 ms. The ion is lost from the trap if one tries to shuttle the ion across the junction in 10s of μs. This effect is presumably due to the ion's acquired kinetic energy after being pushed over an RF hump that leads into the junction region. A faster shuttling time gives the ion too much kinetic energy resulting in the ion being ejected from the trap.

5.3 Corner Shuttling

Shuttling ions around a corner is a non-trivial task because of the existence of RF humps in the pseudopotential near the junction region that are $\sim$0.1 eV high and are about $\sim 200\mu$m in extent. A trapped ion that is doppler cooled to n = 20 has about 10^{-7}eV of energy, so the RF humps are quite significant. It is necessary to push the ion over the RF humps, but in doing so, the ion acquires a lot of kinetic energy. Secondly, creating a potential gradient that is large enough to push the ion over the hump can

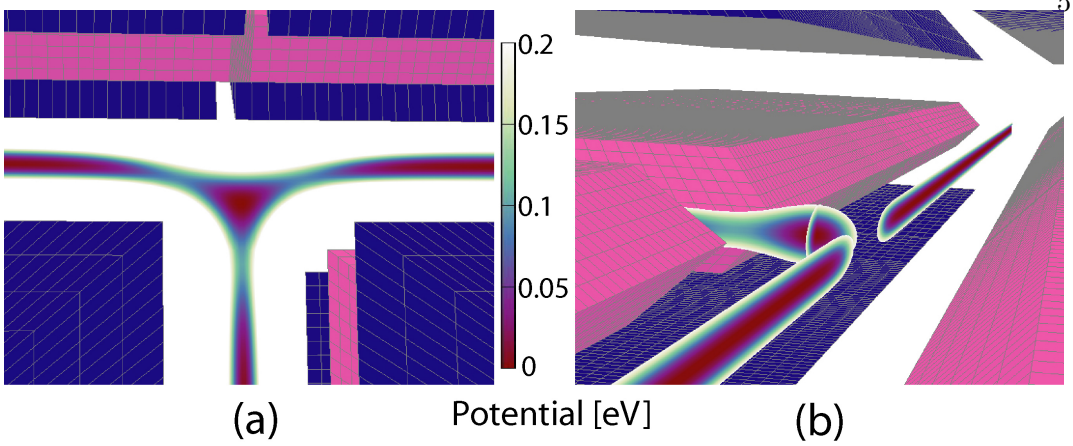

Figure 5.1: RF humps in the potential near the junction of the trap array. The RF humps are ∼1.0 eV high, ∼200 μm in extent, and lead into the T-junction from all three directions. The scale is saturated at 0.2eV. Fig. 5.1b shows a perspective view of the potential looking down the top of the T. This figure also shows a hump in the z-direction so there is no path from the stem to the top of the T that completely avoids the RF hump.

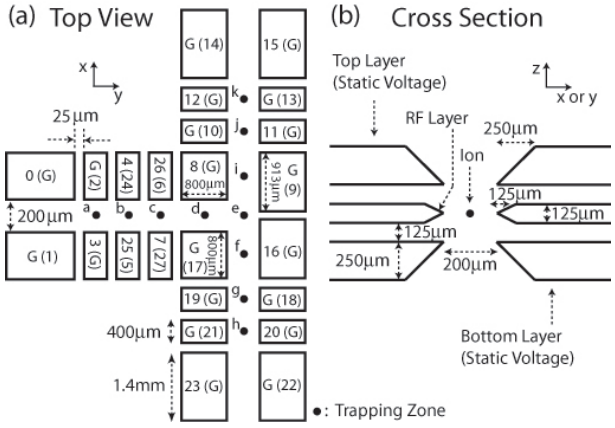

Figure 5.2: T-junction ion trap array schematic. The figure shows all eleven trapping zones labeled a-k. The stem of the T includes zones a-d, while the top includes zones k through h. The control electrodes are numbered and the numbers in brackets indicate the bottom layer. An electrode labeled "G" is grounded. The origin (x,y)=(0, 0) is in the center of the junction near zone e.

destabilize the trap in the transverse direction (in the z-direction).

If an ion is to be shuttled from zone d to zone i, the four most important control electrodes are control electrodes 8, 17, 9, and 16 (see Fig. 5.2). In order to push the ion toward the center of the T-junction (zone e), the voltages of control electrodes 6, 7, 26,

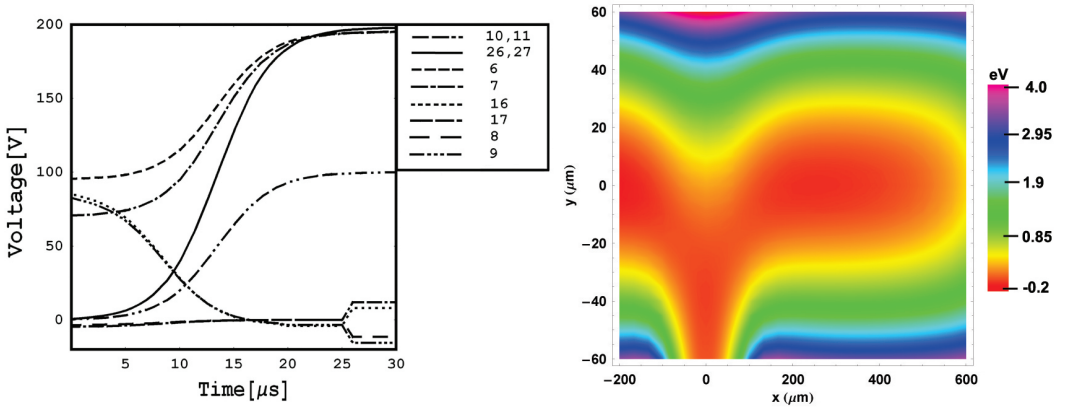

Figure 5.3: The figure on the left is the voltage profile used to shuttle an ion around a corner from zone d to zone i. The control electrode numbers are indicated in the legend. The figure on the right is the pseudo-potential in the trap near the junction at t = 25μs, just before the voltages on electrodes 8, 17, 9, and 16 abruptly change. There is a local maxmimum in the center of the trap, and based on the ion's phase of oscillation, the ion could be on either side of this local maxmimum.

and 27 are simultaneously raised to 200V in 25μs following a hyperbolic tangent time profile (see Fig. 5.3). At the same time, the voltages on control electrodes 8 and 17 are raised from -4V to 0V to provide more potential gradient to force the ion toward zone e. The voltages on control electrodes 9 and 16 are lowered from 80V to -0.3V to pull the ion into the junction.

For the first 16 μs, the ions total energy has increased by approximately 0.1 eV, enough to just scale the RF hump. At t=17 μs, the ion has enough energy to overcome the RF hump, and at t=19 μs, the begins to rapidly pick up kinetic energy as it accelerates toward the junction. The steep potential gradient is necessary because the control electrodes must over write the RF hump, but the voltages on the four junction electrodes need to converge toward a common value so that zone e does not become anti-trapping out of the plane of the T. Because the potential is so flat in zone e and the ion has picked up a lot of kinetic energy going over the RF hump, the ion has a lot of freedom to move in the x-direction. Depending on the initial conditions of the ion, the ion could go either left or right around zone e because there is a local maximum in

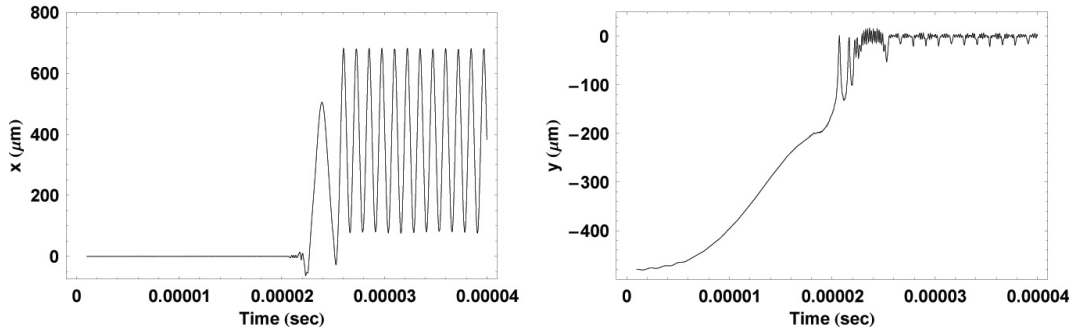

Figure 5.4: Simulated ion motion during corner shuttling when shuttling from zone d to zone i using the Burlish-Stoer method to integrate the ion's equations of motion. The whole shuttling process takes 26μs. The ion acquires a lot of kinetic energy and oscillates wildly in the junction region of the trap becasue the ion enters the relatviely flat potential in the junction after overcoming the RF hump.

the potential until t = 25μs.

The next step toward trapping an ion in zone i is to catch the ion in zone i as it oscillates in the x-direction. As can be seen in Fig. 5.6, the ion has enough kinetic energy to oscillate back and forth between zone i and zone f. Because the phase of this oscillation is unknown during the corner shuttling procedure, catching the ion in zone i while minimizing the acquired kinetic energy is very difficult. However, when simulating the ions motion, care was taken to design a method of catching the ion in zone i so that if the ion is near zone i just after 25μs, the ion will acquire very little kinetic energy as the voltages on control electrodes 16 and 17 are abruptly raised to $\sim$10V while the voltage on control electrodes 8 and 9 decrease abruptly to $\sim$ -10V. The ion would then have approximately 1.0 eV of energy in zone i and could still oscillate over a region of about 400m in the x-direction. Even though the ion has so much kinetic energy, we can image it on a CCD camera because the ion is cooled with a laser that is red-detuned from the $S_{1/2} \rightarrow P_{1/2}$ transition, so the ion does recrystalize. A simulation of the ions motion in the x and y directions can be seen in Fig. 5.4.

The voltages used to shuttle an ion from zone d to zone i create a local maximum in the pseudopotential while the ion is in the junction region as can be seen in Fig. 5.3.

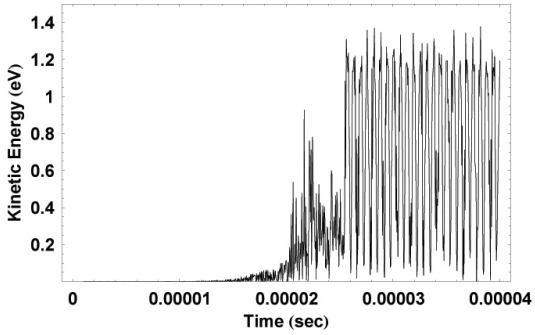

Figure 5.5: Simulation of the acquired kinetic during corner shuttling that takes the ion from zone d to zone i. The ion acquires ∼1.2 eV of kinetic energy during the shuttling process. The ion begins to pick up a lot of kinetic energy after going over the RF hump at t = 17 μs.

This means that the direction the ion begins to oscillate in the junction could either be in the +x or -x direction depending on the phase of oscillation of the ion at the start of the shuttling procedure. Simulations confirm that the ions motion in the junction can go in wildly different directions depending on the phase of oscillation of the ion as it enters the junction region. If the ion ends up going over the potential maximum toward zone f instead of zone i, then at t = 26μs when the voltages rapidly changes, the ion may gain a lot more than than 1 eV of kinetic energy .

There is experimental evidence that this is a real effect. When an ion is shuttled around a corner, the phase of its secular motion in zone d is unknown. This means that the ion can acquire vastly different amounts of kinetic energy during corner shuttling depending on whether or not the ion goes toward zone i or zone f when it intially goes in to the junction region. When the ion leaves the doppler/detection beam in zone d, it can take different amounts of time for the ion to recrystallize in zone i. Despite the fact that the shuttling sequence takes 26 μs, sometimes it takes almost 1 full second for the doppler beam to recrystallize the ion in zone d.

A nice graphical way to illustrate the energy acquired during the corner shuttling process is shown in Fig. 5.6. The evolution of the pseudo-potential as a function of

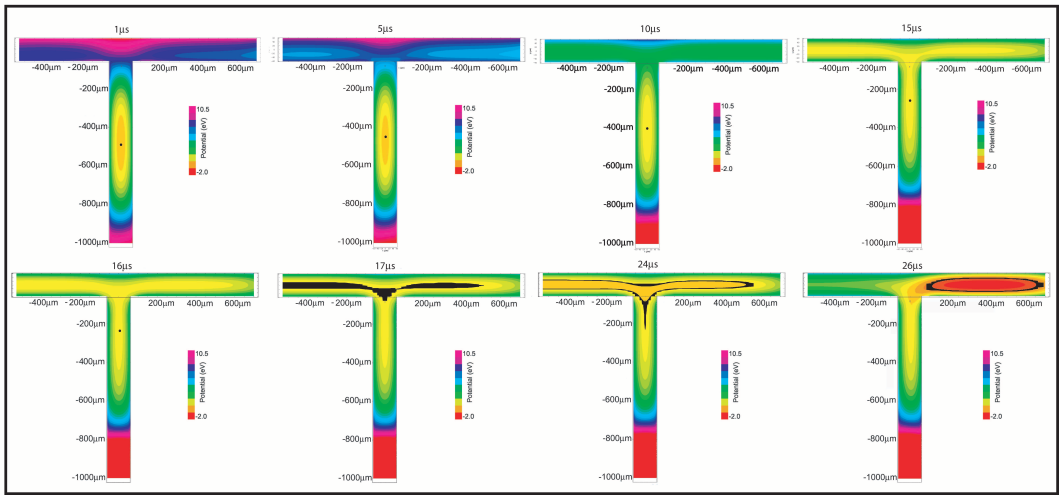

Figure 5.6: Potential energy during a corner shuttling operation that shuttles an ion from zone d to zone i as viewed from the bottom layer of the control electrodes. The black regions indicate regions of the ion trap that the ion is allowed to traverse because it has enough kinetic energy to do so. The black dots at the earlier times during shuttling are not to scale and are meant to give a visual representation where the ion is in the T-trap during the T-trap before the ion acquires a lot of kinetic energy.

the control electrode voltages is shown at different times during the shuttling protocol. The black dots near the beginning of the shuttling protocol indicate the position of the ion. Up until t = 16μs, the ion has gained very little kinetic energy. At t = 17μs, the ion has gained a lot of kinetic energy. This is depicted by the black region in the figure. The enclosed black region represents the areas of the T-junction trap that the ion has enough energy to go if the time evolution of the pseudo-potential were suddenly frozen. The black region has nothing to do with the spread of the wavefunction of the ion because shuttling an ion around the corner in the T-trap is in the classical regime as discussed earlier in this thesis. The corner shuttling operation is over at t = 26μs but the ion has acquired a lot of kinetic energy in the process as is depicted by the wide black ring.

The ion does not always end up with $\sim$1.0eV of energy though, because as the final voltages rapidly rise to try to catch the ion, they can actually give the ion more kinetic energy because the ion experiences an electric field gradient for a longer amount

of time. Simulations show that the ion will still be forced toward zone i, but the amount of kinetic energy acquired will be much larger. Altough the ion is nearly always successfully shuttled around the corner (>99.9% success rate with >1000 attempts), there is experimental evidence that the ion acquires a different amount of kinetic energy during the shuttling process. There is a noticeable difference in the amount of time it takes the ion to recrystallize in zone i after it has left the doppler beam in zone d. The amount of time it takes to recrystallize the ion depends on how much kinetic energy the ion has.

Shuttling back from zone i to zone d is not as straightforward as reversing the control electrode voltage program in time for several reasons. Although Newton's equations are symmetric in time, the ion acquires a lot of kinetic energy upon forward shuttling. The negative of the ion's initial momentum vector when starting in zone i is not even close to the the ion's final momentum vector after being shuttled from zone d to zone i. The geometry of the T-trap does not allow for a simple permutation of electrode control voltages to shuttle back from zone i to zone d based on the control voltage scheme used to shuttle from zone d to zone i. When shuttling from zone d to zone i, the ion can run into the very steep RF potential at the very top of the T-junction (to the right of zone e in Fig. 5.2). When shuttling from zone i to zone e, there is no RF layer for the ion to run straight in to. Lastly, there is a misalignment of the three layers in the T-trap due to the manual assembly process. This misalignment manifests itself in the fact that spatially reflecting the voltage sequence used to shuttle an ion from zone d to zone i does will not successfully shuttle the ion to zone f. It is still possible to shuttle an ion from zone i to zone d with near unit efficiency, but the shuttling time is much longer; it takes 20 ms to shuttle from zone i to zone d as compared to the 26 μs it takes to shuttle from zone d to zone i. Optimizing the shuttling scheme to go from zone i to zone d is still being researched.

None of the corner turning protocols that have succeeded thus far are expected

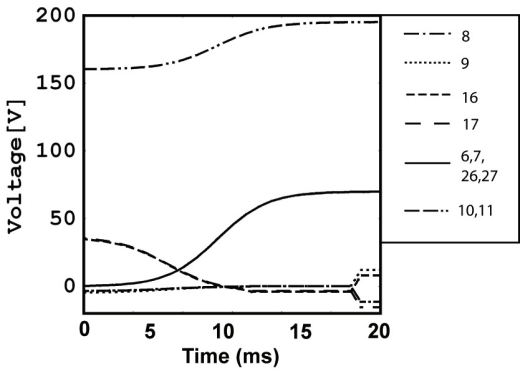

Figure 5.7: Reverse corner shuttling voltage profile to shuttle an ion from zone d to zone i. This shuttling protocol has near unit efficiency but takes almost 10^3 times longer than it takes to shuttle from zone i to zone d. There is no straightforward way to adopt the voltage scheme used to shuttle an ion from zone d to zone i in order to shuttle from zone i to zone d. This is due to the large amount of kinetic energy acquired during the forward shuttling process, the geometrical asymmetry between forward and reverse shuttling, and the misalignment of the three electrode layers relative to each other owing to the manual assembly process.

to be adiabatic with this ion trap geometry. The main reason that it is not possible to smoothly transport ions through the junction region is because of the RF humps. Understanding the scaling of the RF humps as a function ion trap array geometry will be crucial for designing adiabatic corner shuttling processes.

5.4 Separation and Recombination

Two ions that are in the same trapping zone can be separated from each other and shuttled to two different trapping zones by slowly bringing up a potential wedge in between the two ions. The secular frequency decreases from ∼1 MHz to only ∼20 kHz during this process as the potential wedge is brought up between the two ions. The efficiency of separation is only 58% if two ions are separated in 10 ms, but the separation voltage control sequence has not yet been optimized. The T-trap may be fundamentally limited in its ability to separate two ions because the smallest electrodes are 400μm wide [48]. Previous ion separation experiments have been carried out where

ions were separated with near unit efficiency [10] using a small separation electrode that was 100μm wide.

Ions that are initially in different trapping zones can be brought together in the same trap by reverse the separation protocol in time. This has been done experimentally in the T trap and works with near unit efficiency, but if the requirement is made that the ions cannot switch places during the shuttling protocol, then the probability of success is ~ 40 %.

5.5 Swapping

Linear shuttling, corner shuttling, separation, and recombination protocols may be combined to swap the positions of two ions that are initially trapped in the same trapping zone. The step-wise process is depicted in Fig. 5.8. Two ions are initially trapped in zone d, and in order to tell that the two ions have successfully swapped positions, two different isotopes of cadmium ions are trapped in zone d. The two different isotopes have different $S_{1/2}$ to $P_{3/2}$ resonance frequencies, so the ions scatter a different number of photons when a detection laser is incident upon them. The difference in photon scattering can be seen in the first panel of Fig. 5.8.

The ions are shuttled to zone b where they are separated by a potential wedge comes up and separates the ions. One ion is shuttled to zone a while the other is shuttled back to zone d where it is doppler cooled. The ion is then shuttled around the corner of the T-junction from zone d to zone i after which it is linearly shuttled to zone k (step 3 of Fig. 5.8) while the other ion is shuttled from zone a to zone d where it is doppler cooled. The ion in zone d is then shuttled to zone i (where the ion is again doppler cooled) after which it is shuttled through the junction to zone f. As of the time of the writing of this thesis, attempts to shuttle ions around the corner from zone d to directly to zone f have proven unsuccessful owing to the electrode misalignment of the three layers of the T-junction trap array. The ion in zone f is linearly shuttled to zone h. Ion

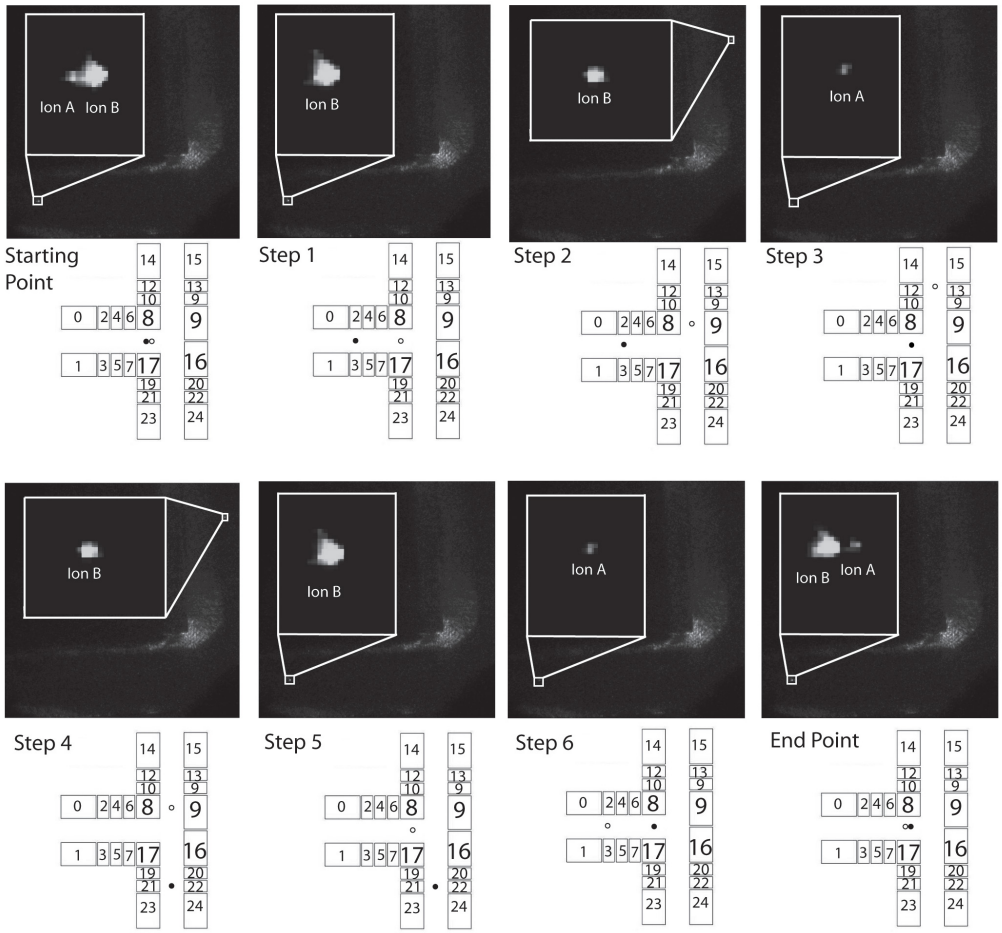

Figure 5.8: Diagram of experimentally demonstrated ion swapping. Two ions are initially trapped in zone d. They scatter a different number of photons because the two ions are different isotopes and thus have two slightly different $S_{1/2}$ to $P_{1/2}$ transitions due to the isotope shift. The ions make a successive three point turn by sending one ion around the corner one way and the other ion around the corner in the other direction. The two ions are brought back in the opposite order so that they have switched places. This protocol makes use of linear shuttling, corner shuttling, separation, and recombination.

B is shuttled back to zone i then to zone d (step 5) where it can be doppler cooled after which it is shuttled to zone a. Ion A is then shuttled from zone h to zone i where it can be doppler cooled, and then Ion B is shuttled to zone d. The ions are then recombined in zone b and shuttled together to zone d where they are doppler cooled and imaged.

The net effect is that the ions have switched places by executing a three point turn in the T-junction ion trap array.

This process is carried out in successive 10 ms steps and has an overall success rate of only 24%, but this is mainly hampered by the 58% success rate of the initial separation attempts and the final recombination attempts. Excluding the separation step at the beginning of the swapping protocol, the success rate of the remaining steps is 82%. Other than a failed separation, the main cause of a failed swapping protocol is that ions can swap places during the recombination step. Note that this protocol is carried out in successive 10 ms steps instead of as a continuous process. The reason that the swapping procedure was tested in a stepwise fashion was to ensure the success of each individual step of the protocol. If the entire protocol was run at once, it would be impossible to tell if the ions were actually separated or not. If the separation step fails, then both ions could be shuttled together and could switch positions during the corner shuttling process. The quoted 82% success rate may also be strongly dependent on Doppler cooling the ions whenever they are in zones d or i. Future work will characterize the success rate these protocols without Doppler cooling beams during the swapping process.

Chapter 6

T-trap Relevance to Quantum Computing

The ion trap stands out as an attractive candidate for making a scalable quantum computer[2],[3]. A hurdle toward realizing such a scalable system with ion traps is the full, two dimensional control of the ions within the trap. Several experiments have demonstrated the shuttling of ions between linearly adjacent trapping zones, the separation of two ions in the same ion trap, and the recombination of two ions into the same trapping zone[48]. These protocols have been successfully used for entanglement[10], implementation of a quantum Fourier transform[11] that is essential for implementing Shor's Algorithm[4], and error correction[49].

There are two major issues to contend with when talking about a scalable geometry. The first is the actual physical layout of the ion trap electrodes. It may be possible to implement calculations using hundreds of trapped ions that are in the same trap or in a separate trapping zones in a linear chain. However, such a geometry requires the use of many pairwise entanglements two entangle ions that are separated by many trapping zones. The ability to sort ions requires at least two dimensional control of trapped ions, so a two dimensional geometry can be considered scalable.

The other aspect to geometrical scalability is the manufacturing process. The first experimental demonstration of two dimensional control of trapped ions by W.K. Hensinger et al [16] was quasi-scalable system because the three layers of the trap were manually aligned above each other. This manual assembly resulted in a misalignment

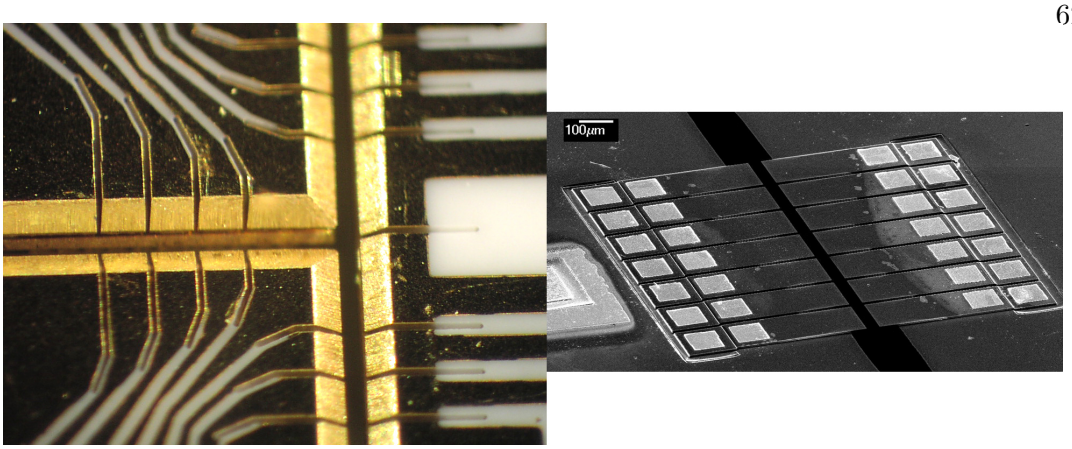

Figure 6.1: A scalable geometry and a scalable manufacturing process: T-junction ion trap array and AlGaAs ion trap. The T-trap is an example of a working trap with a scalable geometry and the AlGaAs trap is an example of a working trap with a scalable manufacturing process.

of the three layers which resulted in a breaking of the symmetry of the T-trap's mirror plane about its C_2 axis. This made it impossible to reflect the necessary voltages profiles of the control electrodes needed to shuttle an ion around a corner to successfully turn the other direction. If hundreds or thousands of ions are to be trapped in a multi-zone ion trap, it may be necessary to have many junctions. If turning the corner of each junction in each direction requires the development of a custom control electrode voltage profile, such a geometry cannot be said to be scalable. An example of a scalable trap manufacturing process that was successfully used to trap individual ions was first demonstrated using an AlGaAs trap in a seminal experiment by D. Stick et al [15]. Fig. 6.1 shows both the T-trap where a proof of principle experiment was performed to show that ions can be controlled in two dimensions, and the AlGaAs trap where a proof of principle experiment was performed showing that ions can be trapped and linearly shuttled in a trap made using semiconductor etching techniques.

There are other aspects to scalable manufacturing prcesses as well; as the number of trap electrodes increases, it becomes increasingly more difficult to wire up all of the electrodes and filters. The greater challenge lies in designing automated sequences to

simulate the potential and work out how the voltages should be optimally changed so that arbitrarily long and complex shuttling operations can be carried out.

Bibliography

[1] J.I. Cirac, P. Zoller. Phys. Rev. Lett. 74, 20 (1995).

[2] D. Kielpinski, C. Monroe, and D. J. Wineland, Nature 417, 709 (2002).

[3] A. M. Steane, quant-ph/0412165.

[4] Shor, Peter W. SIAM Journal on Computing. 1997. 26(5). 1484-1509.

[5] D. Deutsch. Proc. Roy. Soc. London Ser. A. 400, 97 (1985).

[6] I.L. Chuang, M.A. Nielsen. Quantum Computation and Quantum Information. Cambridge University Press. Cambridge, MA. 2000. Pg. 7.

[7] D.P. DiVincenzo. Fortschritte der Physik, 48, 771-783, (2000).

[8] K.-A. Brickman, P.C. Haljan, P.J. Lee, M. Acton, L. Deslauriers, C. Monroe. Phys. Rev. A 72, 050306(R) (2005).

[9] H. Haffner, W. Hansel, C.F. Roos, J. Benhelm, D. Chek-al-kar, T. Korber, U.D. Rapol, M. Riebe, P.O. Schmidt, C. Becher, O. Guhne, W. Dur, R. Blatt. Nature 438, 643-646. (2005).

[10] M.D. Barrett, J. Chiaverini, T. Schaetz, J. Britton, W. M. Itano, J.D. Jost, E. Knill, C. Langer, D. Leibfried, R. Ozeri, and D. J. Wineland, Nature 429, 737 (2004).

[11] J. Chiaverini, J. Britton, D. Leibfried, E. Knill, M. D. Barrett, R.B. Blakestad, W.M. Itano, J.D. Jost, C. Langer, R. Ozeri, T. Schaetz, and D.J. Wineland, Science 308, 997 (2005).

[12] P.C. Haljan, P.J. Lee, K.-A. Brickman, L. Deslauriers, C. Monroe. Phys. Rev. A 72, 062316 (2005).

[13] M. Acton, K.-A. Brickman, P.C. Haljan, P.J. Lee, L. Deslauriers, C. Monroe. quant-ph/0511257 (2005).

[14] C. Langer, R. Ozeri, J.D. Jost, J. Chiaverini, B. DeMarco, A. Ben-Kish, R.B. Blakestad, J. Britton, D.B Hume, W.M. Itano, D. Leibfried, R. Reichle, T. Rosenband, T. Schaetz, P.O. Schmidt, D.J. Wineland. Phys. Rev. Lett. 95, 060502 (2005).

[15] D. Stick, W.K. Hensinger, S. Olmschenk, M.J. Madsen, K. Schwab, C. Monroe. Nature Physics 2, 36 (2006).

[16] W.K. Hensinger, S. Olmschenk, D. Stick, D. Hucul, M. Yeo, M. Acton, L. Deslauriers, C. Monroe, J Rabchuk. App. Phys. Lett. 88, 034101 (2006).

[17] B.B. Blinov, D.L. Moehring, L.-M. Duan, C. Monroe. Nature 428, 153-157 (2004).

[18] S. Seidelin, J. Chiaverini, R. Reichle, J.J. Bollinger, D. Leibfried, J. Britton, J.H. Wesenberg, R.B. Blakestad, R.J. Epstein, D.B. Hume, J.D. Jost, C. Langer, R. Ozeri, N. Shiga, D.J. Wineland. quant-ph/0601173.

[19] H.G. Dehmelt. Adv. At. Mol. Phys. 3, 53 (1967).

[20] Abromowitz, M; Stegun, I.A. Handbook of Mathematical Functions. US Department of Commerce National Bureau of Standards. Applied Mathematics Series 55. 1964; Ch. 20.

[21] R.I. Thompson, T.J. Harmon, M.G. Ball. Canadian Journal of Physics; Dec 2002; 80, 12. pg. 1433.

[22] W. Paul. Proc. International School of Physics Enrico Fermi. 9-19 July 1991. Amesterdam, NY. 1992 pg. 497-517.

[23] Jackson, John D. Classical Electrodynamics. 3rd ed. John Wiley & Sons, Inc. Hoboken, NJ. 1999; Pg. 39.

[24] Cohen-Tannoudji, Claude; Diu, Bernard; Laloe, Franck. Quantum Mechanics vol II. John Wiley and Sons. New York, NY. 1977. Pg. 1110.

[25] W.K. Hensinger, N.R. Heckenberg, G.J. Milburn, H. Rubinsztein-Dunlop, J. Opt. B: Quantum Semiclass. Opt. 5, R83 (2003).

[26] Press, William H; Teukolsky, Saul A; Vetterling, William T; Flannery, Brian P. Numerical Recipes in C: The Art of Scientific Computing. 2nd ed. Cambridge University Press. New York, NY. 2002. Ch. 16.

[27] Yeo, M. Undegraduate Honors Thesis. University of Michigan. 2006.

[28] Griffiths, David J. Introduction of Quantum Mechanics. Prentice Hall Inc. Upper Saddle River, NJ. 1995. Pg. 327.

[29] D.J. Wineland, C. Monroe, W.M. Itano, D. Leibfried, D.E. King, D.M. Meekhof. Journal of Research of the National Institute of Standards and Technology. 103, 259 (1998).

[30] L. Deslauriers, P.C. Haljan, P.J. Lee, K.-A. Brickman, B.B. Blinov, M.J. Madsen, C. Monroe. Phys. Rev. A 70, 043408 (2004).

[31] Q.A. Turchette, D. Kielpinski, B.E. King, D. Leibfried, D.M. Meekhof, C.J. Myatt, M.A. Rowe, C.A. Sackett, C.S. Wood, W.M. Itano, C. Monroe, D.J. Wineland. Phys. Rev. A 61, 063418-8 (2000).

[32] *"Efficient Photoionization-Loading of Trapped Cadmium Ions with Ultrafast Pulses,"* L. Deslauriers, M. Acton, B.B. Blinov, K.-A. Brickman, P.C. Haljan, W.K. Hensinger, D. Hucul, S. Katnik, R.N Kohn, P.J. Lee, M. A. Madsen, P. Maunz, D.L. Moehring, S. Olmschenk, D. Stick, C. Monroe. (submitted, 2006).

[33] A. Kastler. J. Phys. Rad. 11, 255 (1950).

[34] Metcalf, Harold J.; van der Straten, Peter. Laser Cooling and Trapping. Springer-Verlag New York Inc. New York, NY. 1999. Ch. 6.

[35] J.I. Cirac and P. Zoller. Phys. Rev. Lett. 74, 4091 (2004).

[36] K.Molmer, A. Sorensen. Phys. Rev. Lett. 82, 1835 (1999).

[37] G.J. Milburn, S. Schneider, D.F.V. James. Fortschr. Physik 48, 801 (2000).

[38] D.J. Wineland et al. NIST J. Res. 103, 259 (1998).

[39] Q.A. Turchette et al. Phys. Rev. A 61, 063418 (2000).

[40] L. Deslauriers et al. Phys. Rev. A 70, 043408 (2004).

[41] L. Deslauriers, S. Olmschenk, D. Stick, W.K. Hensinger, J. Sterk, C. Monroe. quant-ph/0602003.

[42] A.R. Peaker, U. Kaufmann, Z.-G. Wang, R. Worner, B. Hamilton, H.G. Grimmeiss. J. Phys. C: Solid State Phys. 17, 6161-6167 (1984).

[43] B. Predel, Au-Ba (Gold-Barium), Landolt-Bornstein - Group IV Physical Chemistry, Vol. 5, Issue 1, Jan 1991.

[44] M.A. George. PhD Thesis Arizona State University. Disseration Abstracts International, Vol 52-11, B, 5904 (1991).

[45] A. Olander. Journal Am. Chem. Soc. 54, 10, 3819 (1932).

[46] B. Predel, Au-Ca (Gold-Calcium), Landolt-Brnstein - Group IV Physical Chemistry, Vol. 5, Issue 1, Jan 1991.

[47] V.O. Heinen. PhD Thesis Michigan State University. Dissertation Abstracts International, Vol. 44-09, B, 2803 (1983).

[48] M. A. Rowe, A. Ben-Kish, B. DeMarco, D. Leibfried, V. Meyer, J. Beall, J. Britton, J. Hughes, W. M. Itano, B. Jelenkovic, C. Langer, T. Rosenband, and D. J. Wineland, Quantum Information and Computation 2, 257-271 (2002).

[49] J. Chiaverini, D. Leibfried, T. Schaetz, M. D. Barrett, R. B. Blakestad, J. Britton, W.M. Itano, J.D. Jost, E. Knill, C. Langer, R. Ozeri, and D.J. Wineland, Nature 432, 602(2004).